論文 / 著書情報
Article / Book Information

Title	Effect of suffusion and self-filtration on mechanical behavior of well-graded sands
Authors	Jitrakon Prasomsri, Ratamanee Nuntasarn, Suched Likitlersuang, Akihiro Takahashi
Citation	Soils and Foundations, Vol. 65, Issue 3, 101622
Pub. date	2025, 6
DOI	https://doi.org/10.1016/j.sandf.2025.101622
Creative Commons	Information is in the article.

HOSTED BY

ELSEVIER

Available online at www.sciencedirect.com

ScienceDirect

Soils and Foundations 65 (2025) 101622

www.elsevier.com/locate/sandf

Technical Paper

Effect of suffusion and self-filtration on mechanical behavior of well-graded sands

Jitrakon Prasomsri [a], Ratamanee Nuntasarn [a], Suched Likitlersuang [b], Akihiro Takahashi [c,*]

[a] *Sustainable Infrastructure Research and Development Center, Department of Civil Engineering, Faculty of Engineering, Khon Kaen University, Khon Kaen 40002, Thailand*

[b] *Centre of Excellence in Geotechnical and Geoenvironmental Engineering, Department of Civil Engineering, Faculty of Engineering, Chulalongkorn University, Bangkok, Thailand*

[c] *Department of Civil and Environmental Engineering, Institute of Science Tokyo, Tokyo, Japan*

Received 16 November 2024; received in revised form 25 March 2025; accepted 7 April 2025

Abstract

Suffusion in well-graded sands is a significant concern in geotechnical engineering, potentially leading to malfunctions or failures in soil slopes, earth dams, and their foundations. In this paper, two internally unstable well-graded sands of various densities are subjected to seepage tests and consolidated undrained triaxial compression tests using an in-house developed triaxial permeameter. The tests explore the impact of the uniformity coefficient (C_u), initial density, and hydraulic loading amplitude on suffusion. The effect of suffusion on the undrained mechanical behavior is investigated. The results indicate that specimens with smaller C_u and higher density exhibit a larger onset hydraulic gradient for suffusion, resulting in a smaller eroded mass and fewer changes in permeability. Increasing the hydraulic loading amplitude leads to a larger eroded mass and more changes in permeability. Compared to non-eroded specimens, eroded specimens exhibit reduced shear strength and stiffness during compression tests, increased strain-softening, and contractive behavior. A post-test particle-size distribution analysis shows a significant increase in particles smaller than 0.425 mm within the eroded specimens' mid-section, in contrast to a reduction in the top section. This leads to clogging in the midsection, due to seepage, and a non-uniform particle-size distribution throughout the specimens. Suffusion also causes a decrease in mean effective stress at the critical state in the specific volume-mean effective stress plane.

Keywords: Seepage; Suffusion; Erosion; Permeability; Shear strength

1. Introduction

Suffusion, or internal instability, is one of the internal erosion mechanisms that has been described by the loss of integrity of soils by seepage flow and is associated with the transportation of finer particles in internally unstable soils. As the finer particles are carried away, they may become trapped within the soil mass, forming a filter interface that can prevent further erosion, resulting in a decrease in permeability and erosion rate. This process is defined as self-filtration. Internal erosion has been identified as a key factor in the malfunctions or failures of numerous aging earthen structures, such as soil slopes, earth dams, and their foundations. Some examples of internal erosion-induced failures and malfunctions in natural soil deposits and earthen structures have been reported in the literature (e.g., Stewart and Watts, 2000; Fell et al.,

* Corresponding author at: Department of Civil and Environmental Engineering, Institute of Science Tokyo, 2-12-1 Oh-okayama, Meguro, Tokyo, Japan.

E-mail addresses: jitrpra@kku.ac.th (J. Prasomsri), nratam@kku.ac.th (R. Nuntasarn), fceslk@eng.chula.ac.th (S. Likitlersuang), takahashi.a.3a81@m.isct.ac.jp (A. Takahashi).

https://doi.org/10.1016/j.sandf.2025.101622

Nomenclature

A	Average specimen cross-sectional area
C_u	Uniformity coefficient
C_c	Curvature coefficient
CS	Critical state
CSL	Critical state line
D	Particle diameter
E_s	Undrained secant stiffness
e_c	Global void ratio at end of consolidation or before erosion
e_e	Global void ratio after erosion
F	Percentage of mass fraction smaller than particle diameter D
H	Percentage of mass fraction between D and $4D$
H/F	Stability index
$(H/F)_{\min}$	Minimum stability index
h	Height of specimen
IS	Instability state
IL	Instability line
i	Hydraulic gradient
i_e	Suffusion onset hydraulic gradient
k	Average permeability
k_i	Initial permeability
k_e	End-of-test permeability
k^*	Normalized permeability
Δk	Permeability variation
m_e	Eroded soil mass
m_s	Total dry mass
PSD	Particle-size distribution
PT	Phase transformation state
p'	Mean effective stress
p'_i	Initial mean effective stress
$p'_{\min}$	Minimum mean effective stress
p'_p	Mean effective stress at peak deviator stress
p'_{pt}	Mean effective stress at phase transformation state
p'_{cs}	Mean effective stress at critical state
$p'_{cs,n}$	Mean effective stress at CSL of non-eroded soil
$p'_{cs,e}$	Mean effective stress at CSL of eroded soil
$\Delta p'_{cs,e}$	Change in p'_e from CSL of non-eroded soil
Q	Average volumetric flow rate
QS	Quasi-steady state
R_e	Reynolds number
q	Deviator stress
q_p	Deviator stress at peak deviator stress
q_{pt}	Deviator stress at phase transformation state
q_{cs}	Deviator stress at critical state
u	Pore-water pressure
Δu	Differential pore-water pressure
u_{IT}	Inlet tank pore-water pressure
$u_{IT,\ \max}$	Maximum inlet tank pore-water pressure
u_B	Base pore-water pressure
u_T	Top pore-water pressure
u_p	Pore-water pressure at peak deviator stress
u_{pt}	Pore-water pressure at phase transformation state
u_{cs}	Pore-water pressure at critical state
V	Discharge velocity
v	Specific volume
v_c	Specific volume after consolidation
v_e	Specific volume after suffusion
Δv_e	Change in specific volume due to suffusion
ε_a	Axial strain
$\varepsilon_{a,p}$	Axial strain at peak deviator stress
$\varepsilon_{a,pt}$	Axial strain at phase transformation state
$\varepsilon_{a,cs}$	Axial strain at critical state
ε_r	Radial strain
ε_v	Volumetric stain
σ'_a	Effective axial stress
σ'_r	Effective radial stress
γ_w	Unit weight of water

2003; Peng and Zhang, 2012; Yasuda et al., 2016; Razavi et al., 2020).

Civil engineers have shown interest in understanding the changes in soil strength and stress–strain behavior caused by suffusion, as it poses a hidden threat to the stability of earthen structures due to seepage. Numerous experimental studies in the laboratory have been performed to grasp the impact of suffusion on the strength and stress–strain behavior, as listed in Table 1.

Previous studies have shown that suffusion in gap-graded soils leads to changes in mechanical properties such as the strength and stress–strain behavior. For the post-suffusion mechanical properties under drained shearing conditions, research suggests that gap-graded soils experiencing instability exhibit reduced strength and stiffness, and become more contractive (e.g., Chang and Zhang, 2011; Xiao and Shwiyhat, 2012; Ke and Takahashi, 2015; Li et al., 2020; Chen and Zhang, 2023). The previous experiments under drained conditions provide an expected understanding of the impact of suffusion on the strength and stress–strain behavior of soils. However, the findings under undrained conditions are conflicting. While some studies indicate increased strength and stiffness after suffusion (e.g., Ouyang and Takahashi, 2015; Mehdizadeh et al., 2017), others, like Prasomsri and Takahashi (2020), report significant reductions in shear strength, residual strength, and stiffness. This discrepancy highlights the complexity of the issue and the need for further research to fully understand the undrained mechanical behavior of post-suffusion soils.

Table 1
Summary of the selected studies on the effect of suffusion on the mechanical behavior.

Reference	Gradation[a]	Material	Specimen size		Shearing condition[b]	Post-suffusion mechanical behavior	
			Diameter (cm)	Length (cm)		Strength	Contraction
Chang and Zhang (2011)	GG	Sand, Gravel	10	10	D	Decrease	More
Xiao and Shwiyhat (2012)	GG	Clay, Silt, Sand	5	10	D	Decrease	More
Ke and Takahashi (2015)	GG	Sand	7	15	D	Decrease	More
Ouyang and Takahashi (2015)	GG	Sand	7	15	U	Increase	Less
Mehdizadeh et al. (2017)	GG	Sand	5, 7.5, 10	10, 15, 20	U	Increase	Less
Li et al. (2020)	GG	Silt, Sand, Gravel	20	40	D	Decrease	More
Prasomsri and Takahashi (2020)	GG	Sand	7.5	15	U	Decrease	More
Chen and Zhang (2023)	GG	Sand, Gravel	7.6	15	D	Decrease	More
Chitravel et al. (2021)	WG	Silt, Sand	7.5	16	D, U	Increase	Less

[a] GG is gap-graded and WG is well-graded.
[b] D is drained condition and U is undrained condition.

As summarized in Table 1, previous research has primarily concentrated on the suffusion and post-suffusion mechanical behavior in gap-graded soils. However, natural soils and those encountered in civil engineering applications, like earth dam construction, are often well-graded. Nevertheless, the internal stability characteristics of well-graded soils and their impact on the undrained mechanical behavior remain understudied and poorly understood (e.g., Sato and Kuwano, 2016; Chitravel et al., 2021). Therefore, it is of great importance to investigate the factors influencing suffusion characteristics and their impact on the mechanical behavior of well-graded soils.

The aim of this study is to conduct an in-depth investigation of suffusion in well-graded sands and its impact on their mechanical behavior. The study focuses on examining how the initial density, uniformity coefficient, and hydraulic loading amplitude influence suffusion characteristics and, in turn, affect the mechanical behavior. Series of seepage and undrained triaxial shear tests are carried out using an in-house developed triaxial permeameter. The suffusion characteristics (i.e., changes in permeability, volumetric strain, and eroded soil mass), factors influencing suffusion (i.e., initial density, particle-size distribution, and hydraulic loading amplitude), and post-suffusion mechanical responses (i.e., stress–strain behavior, strength, and critical state) are investigated and discussed. By understanding the mechanisms of suffusion and their impact on the material properties of dams, as revealed by the test results, dam engineers and owners will be able to identify and mitigate the risks of internal erosion to ensure the long-term safety and reliability of their dams.

2. Experimental investigation

2.1. Test materials

The present study investigates soil collected from the foundation of a levee along the Kinu River in Jyouso City, Ibaraki Prefecture, Japan. This levee suffered internal erosion during the 2015 Kanto and Tohoku Heavy Rain event (Yasuda et al., 2016), resulting in multiple instances of sand boiling and piping along the downstream area. The foundation soil, composed of loose alluvial sand, was sampled from the boiled sand deposits and used to develop the soil mixtures for this study. The particle-size distribution (PSD) of this in-situ soil is shown in Fig. 1(a). Due to the presence of clay and silt in the in-situ soil, direct erosion testing in the apparatus used in this study was impractical. To overcome this limitation, scaled soil models were created using the parallel gradation method (Varadarajan et al., 2003). Two scaled soils, "K10" and "K20", were developed by scaling the in-situ soil particle sizes by factors of 10 and 20, respectively. The PSDs of these scaled soils are also presented in Fig. 1(a). It is important to note that scaling the particle sizes of a soil can lead to the overestimation of permeability due to increased porosity (Krumbein and Monk, 1943) and a decrease in shear strength with an increasing particle size (Varadarajan et al., 2003).

The scaled soils have the same curvature coefficient (C_c) as the in-situ soil, but different uniformity coefficients (C_u). K10 is classified as silty sand (SM), while K20 is classified as well-graded sand with silt and gravel (SW-SM) according to ASTM D2487-11 (2012). These sands comprise 12 sieve fractions (0.025 mm to 5 mm) from eight non-plastic silica sands (Silica Nos. 1 to 8). The particles are categorized as sub-angular to angular in shape. Both the K10 and K20 soils are deemed internally unstable according to Kenney and Lau (1985, 1986) criteria with a limiting minimum H/F stability index $[(H/F)_{min}]$ of 1 (see Fig. 1(b)), where F is the percentage of mass fraction smaller than diameter D and H is the percentage of mass fraction between D and $4D$. The compaction curves for these modeled soils are obtained using standard Proctor compaction tests and are shown in Fig. 2. Table 2 summarizes the physical properties of the scaled soils.

Defining the "finer fraction" in well-graded soils is challenging due to their continuous particle size distribution. However, Kenney and Lau (1985) proposed the concept

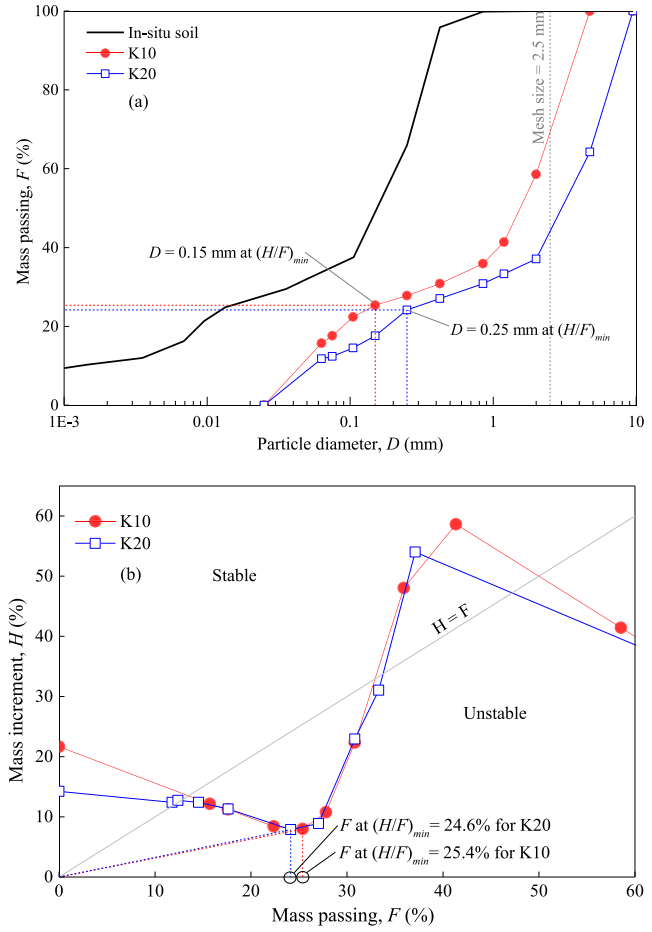

Fig. 1. (a) Particle-size distribution curves, and (b) Kenney and Lau's internal stability criteria.

of the smallest openings (constrictions) of the coarser matrix. These openings are assumed to be one-quarter the size of the finer fraction that can pass through a coarser matrix. This concept forms the basis of the H/F stability index. This study adopts Kenney and Lau's concept to define the "finer fraction" of the K10 and K20 soils, which are particles that might pass through the openings formed by the "coarser fraction". By analyzing the PSDs in Fig. 1 (a), the $(H/F)_{min}$ point for each soil is determined. Particles smaller than the size corresponding to this point are considered the "finer fraction," even if their size exceeds the definition of fines used in ASTM D2487-11 (2012). Conversely, particles larger than the size at the $(H/F)_{min}$ point are classified as the "coarser fraction." This analysis establishes cutoff sizes of 0.15 mm and 0.25 mm for the "finer fractions" in the K10 and K20 soils, respectively.

2.2. Test apparatus

In this study, the modified triaxial permeameter shown in Fig. 3 was developed to conduct continuous seepage tests and subsequent triaxial shear tests. It comprises three key components: a seepage control system, an automated stress-controlled triaxial system, and an eroded soil collection system. The seepage control system, based on an automated pressure-controlled setup, applies the desired hydraulic loading to the soil specimen under confining pressure. The base pedestal is designed to facilitate the collection of eroded soil particles, allowing them to pass through a perforated plate with 2.5-mm-diameter holes and accumulate in the soil collection tank. This tank serves the double purpose of weighing the eroded particles and

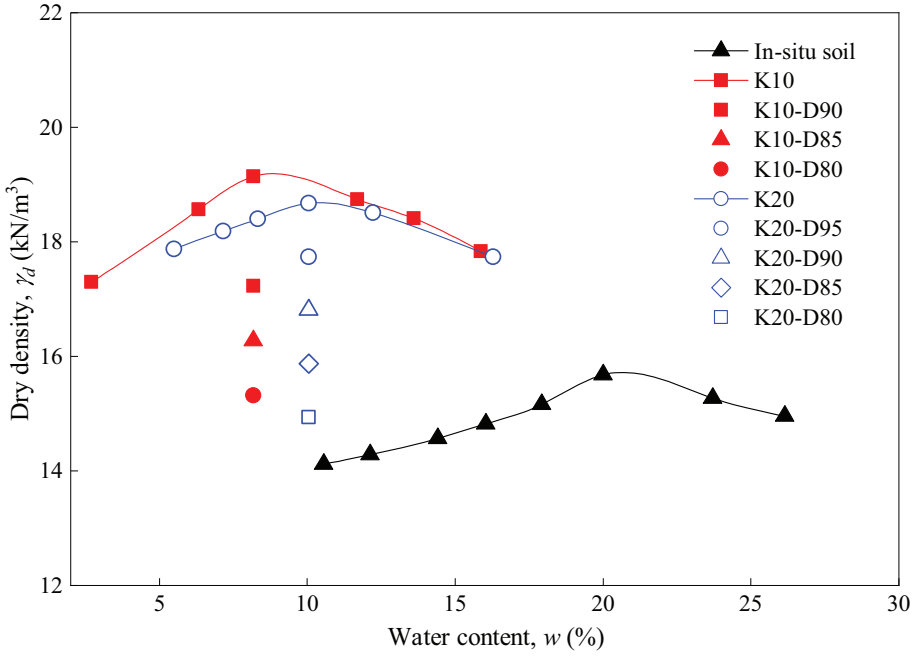

Fig. 2. Compaction characteristics and initial densities of the well-graded soils.

Table 2
Physical properties of the well-graded soils.

Physical property	In-situ soil	Modeled soil	
		K10	K20
D_{95} (mm)	0.42	4.28	8.62
D_{90} (mm)	0.38	3.86	7.83
D_{60} (mm)	0.21	2.06	4.15
Mean particle size, D_{50} (mm)	0.15	1.54	3.02
D_{30} (μm)	38.1	367.6	731.2
D_{15} (μm)	5.6	60.4	110.7
Effective particle size, D_{10} (μm)	1.3	45.0	54.8
D_5 (μm)	0.2	33.6	37.0
Uniformity coefficient, C_u	160.9	45.8	75.7
Curvature coefficient, C_c	5.3	1.5	2.4
Specific gravity, G_s	2.65	2.645	2.645
Maximum dry density, $\gamma_{d,\max}$ (kN/m^3)	15.7	19.1	18.7
Optimum water content, w (%)	20.0	8.2	10.1
$(H/F)_{\min}$	0.3	0.4	0.5
USCS (ASTM D2487-11)	SM	SM	SW-SM
Particle description	–	Sub-angular ~ Angular	

Note: D_x indicates the particle size for which x% of the soil by mass includes particles of that size or smaller.

maintaining the specimen's back pressure during seepage testing to prevent desaturation. Detailed information on the permeameter's design, testing procedure, and test repeatability can be found in the works by Ke and Takahashi (2014), Prasomsri and Takahashi (2020, 2021) and Prasomsri et al. (2021).

2.3. Test procedure and test program

Each test was performed according to the following procedure:

1. Silica sands are mixed to achieve the desired PSDs shown in Fig. 1. Each mixture is moistened to its optimal water content listed in Table 2. Static compaction is then performed using the under-compaction method proposed by Ladd (1978) with the four compaction levels (80 %, 85 %, 90 %, and 95 %) shown in Fig. 2. To ensure specimen uniformity, the Jiang et al. (2003) criterion is used. This criterion involves calculating the required height of each soil layer using the nonlinear average under-compaction equation. The uniformity of each specimen is validated by accessing the distribution of void ratio along its height. The dimensions of the specimens in this study were 150 mm in height and 75 mm in diameter.
2. The specimens are flushed with carbon dioxide for one hour. Saturation is subsequently achieved under a back-pressure of 400 kPa for an additional 10 h. A pore-water pressure B-value greater than 0.95 indicates fully saturated specimens. The specimens are then consolidated to a mean effective stress of 50 kPa.
3. Seepage tests are conducted with downward flow by increasing the inlet tank pore-water pressure (u_{IT}) to its maximum pressure ($u_{IT,\max}$) of 430 or 450 kPa, while maintaining a constant base pore-water pressure (u_B) of 400 kPa. The top pore-water pressure (u_T) is monitored throughout the seepage tests. It is noted that the difference between u_T and u_{IT} represents the head loss that occurs within the fittings and tubes of the system. u_T and u_B are closely attached to the top and bottom of the specimen, respectively. This setup enables the measurement of the changes in flow rate and differential pore-water pressure (Δu) during seepage testing. The deviator stress is kept at zero, allowing each specimen to experience seepage flow under isotropic stress conditions.
4. The specimens are sheared after seepage under undrained conditions at a strain rate of 0.1 %/min until attaining an axial strain of 22 % and reaching the critical state. Corrections are made for cross-sectional area changes and membrane penetration during shearing according to ASTM D4767-11 (2012).
5. The specimens are split into three equal portions, and the PSDs after testing are obtained for both the specimens and the eroded soil retained in the collector.

The average hydraulic gradient (i) for each test is calculated as follows:

$$i = \frac{\Delta u}{\gamma_w h} \tag{1}$$

where Δu represents the differential pore-water pressure between u_T and u_B, h is the height of the specimen, and γ_w is the unit weight of water. The accuracy of u_T and u_B is ±0.1 kPa, leading to an uncertainty in Δu of ±0.14 kPa based on ASTM E2655-08 (2008). Given the ±0.03 % accuracy of the axial strain (ε_a) measurements, the overall uncertainty in i is estimated to be ±0.10 when considering all error sources.

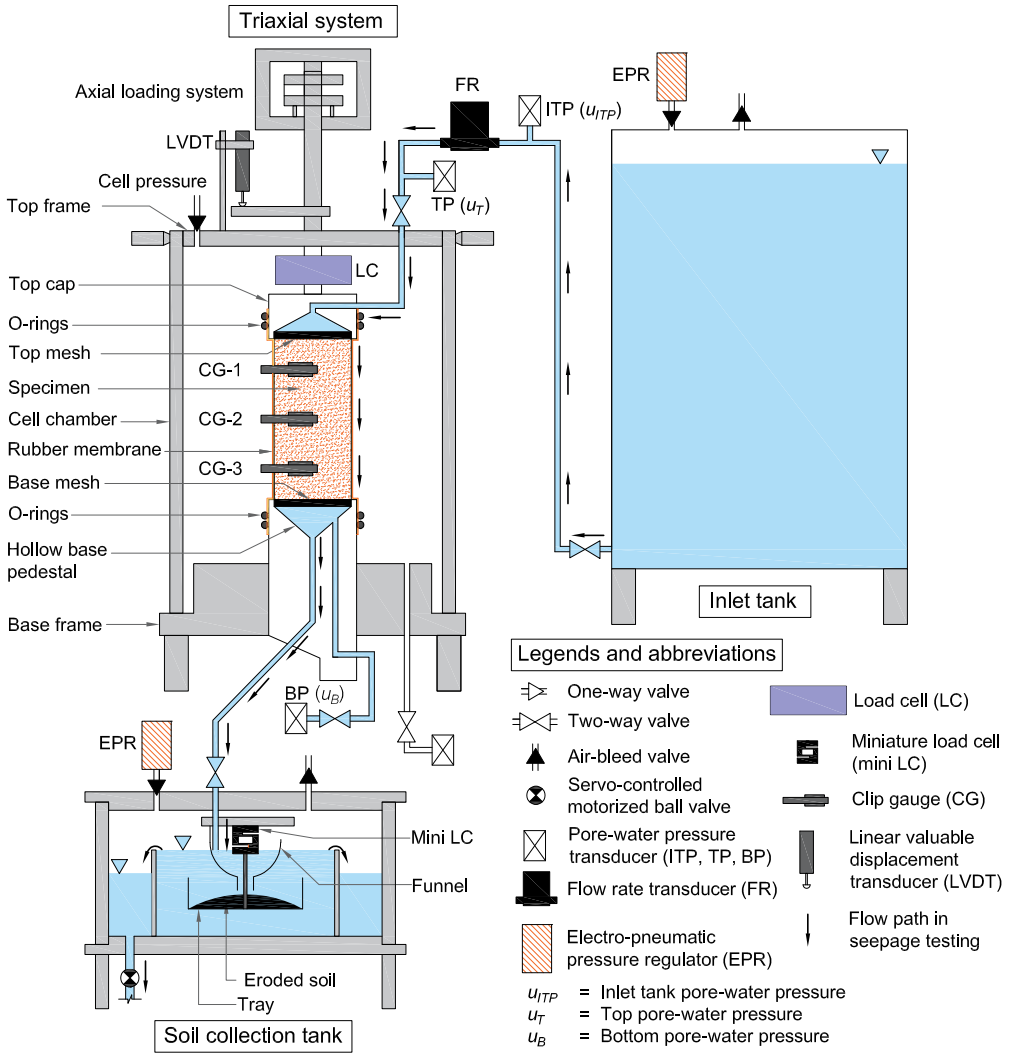

Fig. 3. Schematic diagram of the modified triaxial permeameter.

The discharge volume (V) is determined as follows:

$$V = \frac{Q}{A} \tag{2}$$

where Q is the average volumetric flow rate, and A is the average specimen cross-sectional area, which is calculated based on the average radial displacement from the three clip gauges (CG-1, CG-2, and CG-3) seen in Fig. 3.

The average permeability (k), following Darcy's equation, is calculated as follows:

$$k = \frac{V}{i} \tag{3}$$

The accuracy of Q is $\pm$ 1.33 $\times$ 10^{-9} m^3/s, and the accuracy of the average radial strain (ε_r) measurements is $\pm$0.02 %. Considering all error sources, the overall uncertainty in k is estimated to be $\pm 1 \times 10^{-5}$ m/s.

To quantify the relative changes in permeability caused by suffusion, the normalized permeability (k^*) is introduced here (Johnston et al., 2024) and defined as

$$k^* = \frac{|\Delta k|}{k_i} \tag{4}$$

where Δk is the variation in permeability ($\Delta k = k_e - k_i$), k_e is the end-of-test permeability, and k_i is the initial permeability. It should be noted that k_i is determined from the relationship between i and V. This relationship typically exhibits a constant slope. The greater the k^*, the greater the change in k.

It is noted that permeability is corrected to 20 °C following ASTM D5084-10 (2010). The average volumetric strain (ε_v) is calculated using axial and radial strain measurements ($\varepsilon_v = \varepsilon_a + 2\varepsilon_r$), with an estimated accuracy of $\pm$0.06 %. The eroded soil mass (m_e) is measured using a weighing tray in the collector with an accuracy of $\pm$0.1 g. The parameters observed during the tests are Q, u_{IT}, u_T, u_B, ε_a, ε_r, and m_e, which are continuously monitored. These parameters are continuously recorded at 1-second intervals, which has been shown to provide sufficient resolution for capturing the onset of suffusion (Slangen and Fannin, 2017; Prasomsri et al., 2021).

In this study, the two well-graded soils, K10 and K20, yield the ratio of the specimen diameter to the largest particle size at D_{95} of 17.52 and 8.70, respectively, which are governed by the ASTM standard recommending a minimum ratio of 8 to minimize the preferential flow along the specimen boundaries (ASTM D2434-19, 2019). Additionally, the ratio exceeds the ASTM D7181-20 (2020) minimum requirement of 6, ensuring that the particle size does not influence the triaxial compression test results.

For specimen labels "K10-D90" or "K10-D90-S1", "K10" represents the PSD scaling factor and "D90" represents 90 % of the maximum dry density. "S1" is seepage flow with $u_{IT,\ max}$ of 430 kPa, while "S2" is that with $u_{IT,\ max}$ of 450 kPa as in "K10-D90-S2". "R" indicates a repeated test (e.g., K20-D85-R).

2.4. Visual observation

Fig. 4 displays microscopic images of K10-D90-S2 and K20-D90-S1 after the specimen preparation. These images are used to analyze the specimen's fabric. K10-D90-S2 exhibits sand-silt aggregations, while K20-D90-S1 consists of silt, sand, and gravel. The silt particles, considered the finer fraction (≤0.15 mm or 0.25 mm), are depicted as brighter reflections. The sand and gravel, considered the coarser fraction (>0.15 mm or 0.25 mm), appear darker, but are still visible under the light.

In K10-D90-S2, the finer fraction densely packs around the coarser fraction, while the coarser fraction loses contact. Due to its larger particle sizes and wider PSD, the coarser fraction in K20-D90-S1 acts as the primary load-bearing skeleton, with the finer fraction filling the gaps around it. Other K10 and K20 specimens are compacted with the same gradation as K10-D90-S2 and K20-D90-S1, but at different compaction degrees, resulting in comparable aggregations, but different void ratios.

3. Results and discussion of the seepage tests

3.1. Suffusion characteristics

Suffusion has a direct impact on the permeability and loss of mass of a soil, which can change due to the rearrangement of the soil structure caused by particle movement. According to Prasomsri and Takahashi (2020), the suffusion process involves five states: (1) initial state, in which the permeability is approximately constant without erosion; (2) onset state, which involves the initial detachment of fine particles and changes in permeability; (3) self-filtration state, in which decreased permeability and erosion are observed due to particle clogging; (4) erosion state, in which the significant loss of fine particles and a marked increase in permeability are observed due to the formation of preferential flow paths; and (5) stable state, in which the permeability stabilizes and the erosion rates diminish since the specimens experience a new equilibrium. Importantly, suffusion can occur without any significant volume change, as noted by Fannin and Slangen (2014). To illustrate these characteristics, the K20-D85-S2 specimen will be examined here by analyzing the time histories of k, m_e, and ε_v across the five states, as given in Fig. 5. The variation in k, shown in Fig. 5(c), is derived from the variations in i and V presented in Fig. 5(a) and (b), respectively.

3.1.1. Initial state

For the initial state, the K20-D85-S2 specimen exhibits relatively constant permeability without any significant particle loss or volume change. It yields k_i of 2.2×10^{-4} m/s. The volume change during this stage is negligible since the magnitude is smaller than the measurement accuracy (±0·06 %). The values for k_i for all seepage tests are presented in Table 3 along with the void ratios after consolidation (e_c). It is observed that the values for k_i decrease as e_c decreases. For a given C_u, specimens with comparable e_c, but different C_u, exhibit larger k_i when C_u is larger. The permeability varies based on the fabric, i.e., constriction sizes, and on how the particles are distributed and interconnected, which is linked to the particle-size distribution (represented by C_u) and void ratio (Bandini and Sathiskumar, 2009; Belkhatir et al., 2013).

3.1.2. Onset state

The method presented by Skempton and Brogan (1994) is used to characterize the onset state, in which the suffusion onset hydraulic gradient (i_e) is defined as the minimum gradient that induces changes in permeability and particle loss. As shown in Fig. 5(c) and 5(d), K20-D85-S2 exhibits a decrease in permeability at $t = 1.50$ min, corresponding to $i_e = 1.8$ without any marked change in ε_v. The point at which the hydraulic gradient causes a decrease in k is defined as i_e, as indicated by star symbols in Fig. 5(a). The onset hydraulic gradients for all the tests are given in Table 3. It is noted that the onset of suffusion is defined based on the flow rate measurement, which is taken before the detection of an eroded mass in this experimental setup. This approach helps to minimize discrepancies in the determination of the suffusion onset hydraulic gradient.

3.1.3. Self-filtration state

The self-filtration state is characterized by a decrease in both permeability and erosion rate. For this state, the value of k^* will be used to characterize the amplitude of the self-filtration state. For K20-D85-S2, after the onset of suffusion, k decreases with the subsequent increase in m_e and an insignificant change in ε_v, as indicated in Fig. 5(c) and (d). As seepage continues, the rate of m_e eventually stabilizes, indicating a reduction in erosion. At the end of the seepage test, k^* for K20-D85-S2 reaches 0.55. Similar trends in k and m_e are observed for all tested specimens, although the magnitude of k^* varies. Table 3 also presents the k^* values for all the tests. For all specimens, except K20-D95-S1, the observed variations in permeability exceed the permeability uncertainty ($\pm 1 \times 10^{-5}$ m/s), indi-

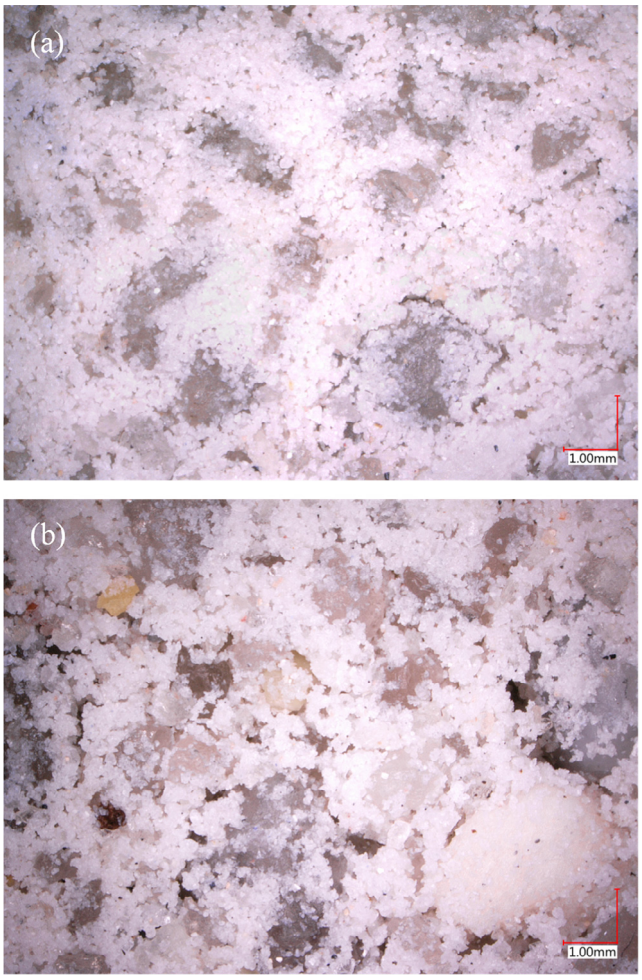

Fig. 4. Microstructures of the well-graded soils after specimen preparation for (a) K10-D90-S2 and (b) K20-D90-S1.

cating significant changes. In contrast, the variation in permeability for K20-D95-S1 (Δk = 2 × 10^{-5} m/s) exhibits a variation that is statistically indistinguishable from the uncertainty threshold, suggesting an insignificant change. This is likely due to the effect of the initial density, which will be discussed below.

3.1.4. Erosion state

The erosion state is characterized by a substantial loss of finer particles and increased permeability resulting from preferential flow paths. However, this erosion state is not observed in the K20-D85-S2 specimen. Instead, self-filtration appears to be the dominant characteristic of suffusion, as previously discussed. This observation extends to the other specimens examined as well.

3.1.5. Stable state

The stable state is defined by the stabilization of permeability and a decrease in the erosion rate. As illustrated in Fig. 5(c) and (d), the K20-D85-S2 specimen reaches the stable state, evidenced by the stabilization of k and m_e towards the end of the test, while ε_v remains negligible. Similar trends are observed for all specimens. At the end of the seepage test, the end-of-test permeability (k_e) for K20-D85-S2 is 1.0 × 10^{-4} m/s, with m_e of 10.3 g. This results in a minimal change in the global void ratio from the initial value before seepage (e_c) of 0.60 to the final value after seepage (e_e) of 0.61.

Table 3 summarizes the key parameters at the initial conditions and after suffusion. In general, the onset of suffusion in well-graded soils occurs rapidly, typically within a few minutes after the onset at i_e of 2.2–5.6. The cumulative eroded soil mass increases rapidly in the early seepage stage, but eventually stabilizes and converges to a constant value towards the end of the test, while the volume change remains insignificant. Based on Foster and Fell (2001) and Douglas et al. (2019) (refer to Table 4), the eroded mass for most tests falls within the minor erosion class, ranging from 0.35 % to 0.96 % of the specimen's total mass. However, test K20-D95-S1 exhibits very minor erosion, with only 0.12 % of the specimen eroded.

In most tests, the significant decrease in permeability and the minor erosion suggest that the detached particles are mainly clogged within the specimen. Clogged layers are formed and the imposed hydraulic gradient is insufficient to break the clogged pores, resulting in constant permeability and a constant erosion rate in the final period of the test. The occurrence of clogging is due to the entrapment and accumulation of detached particles during seepage (Lafleur and Nguyen, 2007; Le et al., 2018; Zhong et al., 2018).

Most of the tested specimens exhibit internal instability, characterized by an initial period of constant permeability, followed by a significant decrease in permeability and a subsequent increase in eroded mass without any significant change in volume. This behavior is indicative of suffusion followed by self-filtration. However, the K20-D95-S1 specimen shows insignificant changes in both permeability and the eroded mass, suggesting internal stability.

The consistency of the specimen preparation and seepage testing procedures can be evaluated by comparing k_i between two specimens with comparable C_u and e_c, namely, K10-D90-S1 and K10-D90-S2, as shown in Fig. 5. These values exhibit minimal variations in both magnitude and trend, suggesting good repeatability in the experimental approach.

3.2. Effect of initial density

The seepage results show that initial density, C_u and the hydraulic load amplitude play significant roles in influencing the characteristics of suffusion. Subsequent sections will investigate the influence of these factors on instability through an analysis of the key seepage parameters, such as i_e, m_e, ε_v, and k*.

The effect of the initial density on suffusion is investigated for the K10 and K20 soils using K10-D80-S1 and K10-D90-S1, and K20-D90-S1 and K20-D95-S1, respectively. Both series share comparable PSDs and hydraulic

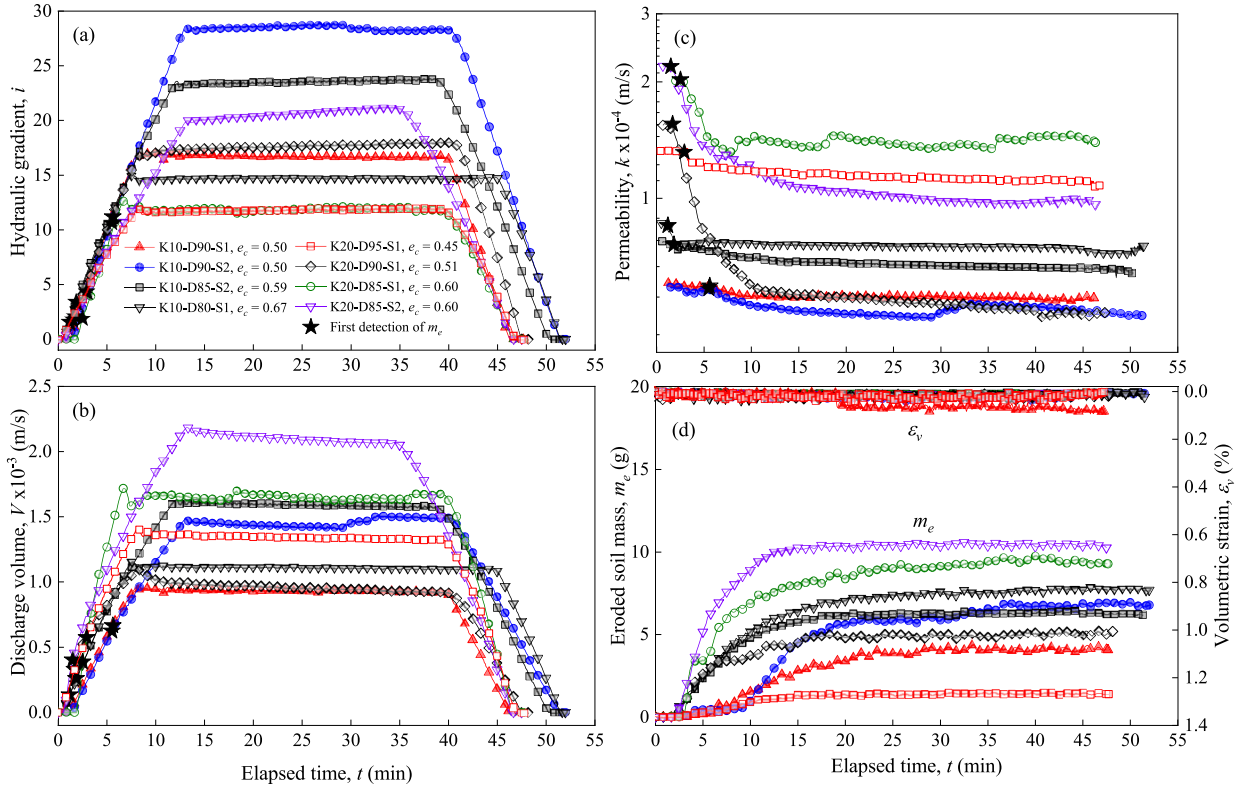

Fig. 5. Time histories of (a) hydraulic gradient, (b) discharge volume, (c) permeability, and (d) eroded soil mass and volumetric strain of the eroded specimens.

Table 3
Summary of the major parameters in the tests.

Test code	Initial and onset conditions						End-of-test conditions					Erosion mode[c]	Erosion class
	m_s (g)	*B*-value	p'_i (kPa)	e_c	k_i (m/s)	i_e	m_e (g)	ε_v (%)	e_e	k_e (m/s)	k^*		
K10-D80-S1	1034.5	0.99	50	0.67	8.6E-05	1.6	7.7	0.02	0.68	7.5E-05	0.13	SF, SU	Minor
K10-D85-S2	1099.1	0.97	50	0.59	7.7E-05	3.4	6.2	0.01	0.60	6.4E-05	0.17	SF, SU	Minor
K10-D90-S1	1163.8	1.00	50	0.50	6.0E-05	11.2	4.1	0.08	0.51	5.5E-05	0.08	SF, SU	Minor
K10-D90-S2	1163.8	1.00	50	0.50	5.9E-05	10.7	6.8	0.01	0.51	5.0E-05	0.15	SF, SU	Minor
K20-D85-S1	1072.3	1.00	50	0.60	2.0E-04	1.9	9.3	0.01	0.62	1.4E-04	0.30	SF, SU	Minor
K20-D85-S2	1072.3	1.00	50	0.60	2.2E-04	1.8	10.3	0.01	0.61	1.0E-04	0.55	SF, SU	Minor
K20-D90-S1	1135.3	1.00	50	0.51	1.5E-04	2.1	5.2	0.02	0.52	5.0E-05	0.67	SF, SU	Minor
K20-D95-S1	1198.4	0.99	50	0.45	1.3E-04	4.4	1.4	0.01	0.46	1.1E-04	0.15	SF, SU	Very minor

[c] SF is self-filtering and SU is suffusion

load amplitudes, but are different in their e_c. Fig. 6 presents the observed changes in k^* and m_e for each specimen, with the corresponding e_c indicated.

An analysis of the K10 tests confirms that increased initial density, demonstrated by the K10-D90-S1 specimen ($e_c = 0.50$), leads to a larger i_e characterized by a smaller m_e and lower k^*. Conversely, the looser K10-D80-S1 specimen ($e_c = 0.67$) exhibits smaller i_e with larger m_e and k^*. Similar trends are observed in the K20 tests with the K20-D90-S1 and K20-D95-S1 specimens. These results highlight the crucial role of soil compaction in both the triggering and the development of suffusion. They align with earlier experimental and numerical studies (Wan and Fell, 2004; Nguyen and Indraratna, 2020; Li et al., 2024), suggesting that denser soils experience stronger inter-particle locking, improved stress transmission, reduced particle detachment, and fewer constrictions in terms of particle movement, collectively diminishing suffusion susceptibility.

Additionally, an increase in density increases the load carried by the finer fraction, thereby enhancing resistance to the onset of suffusion (Shire et al., 2014). Soil permeability, flow rate, and hydraulic velocity are strongly influenced by the void ratio. Higher void ratios lead to increased flow rates, velocities, and accelerated suffusion. As the flow velocity increases, so does the shear stress exerted by the

Table 4
Definition of the erosion classes based on Foster and Fell (2001) and Douglas et al. (2019).

Erosion class	Erosion amount
No erosion	No erosion or only a few grams falling from the mesh when first wetted
Very minor erosion	≤0.2 % of total specimen dry weight
Minor erosion	>0.2 % and <1 % of total specimen dry weight
Medium erosion	1 %–5 % of total specimen dry weight
Major erosion	>5% of total specimen dry weight or 1 %–5 % of the total specimen dry weight but ≥10 % of the dry weight of the finer fraction

water on potentially erodible soil particles. A particle Reynolds number (R_e) also correlates with the potential for particle detachment and transport through the soil. If the particle Reynolds number is relatively large, the lift and virtual mass forces surpass the drag force, leading to particle detachment and transport (Kafui et al., 2002; Yin et al., 2021). Further investigation is needed to fully understand this relationship.

3.3. Effect of uniformity coefficient

The effect of C_u on the suffusion of the two well-graded soils is investigated. Two pairs of soil specimens, K10-D85-S2 and K20-D85-S2, and K10-D90-S1 and K20-D90-S1, are analyzed. Notably, these specimens share comparable void ratios, hydraulic load amplitudes, and effective stresses, but differ in their C_u values. Fig. 7 depicts the impact of C_u on the seepage response, highlighting the e_c and C_u values for each specimen.

As anticipated, the specimens with smaller C_u exhibit smaller m_e, smaller k^*, and larger i_e. Conversely, the specimens with larger C_u demonstrate larger m_e, larger k^*, and smaller i_e. These findings suggest that soils with larger C_u are more susceptible to suffusion, initiating at a smaller hydraulic gradient. Once suffusion begins, the soils with larger C_u exhibit greater erosion and changes in permeability. This observation aligns with prior experimental and numerical studies (Nguyen and Indraratna, 2020; Li et al., 2024). In soils with larger C_u, the coarser particles within the primary fabric provide load support and stress transmission within the soils, leading to larger and more distributed constriction voids. These voids permit easier migration of detached particles without stress transfer, eventually decreasing resistance to suffusion.

3.4. Effect of hydraulic loading

Fig. 8 depicts the impact of the hydraulic loading amplitude on suffusion by comparing K10-D90-S1 and K10-D90-S2 in the K10 tests, and K20-D85-S1 and K20-D85-S2 in the K20 tests. These specimens share identical particle-size distributions and initial densities, with the only difference being their hydraulic load amplitudes ($u_{ITP,\ max}$).

The results reveal that specimens subjected to larger hydraulic loads (K10-D90-S2 and K20-D85-S2) exhibit larger m_e and k^* compared to their counterparts with smaller hydraulic loads (K10-D90-S1 and K20-D85-S1). This suggests that increasing the hydraulic load amplitude will lead to a larger eroded mass and larger relative permeability, indicating greater suffusion potential. These findings align with prior studies by Sibille et al. (2015), Rochim et al. (2017), and Li et al. (2024). A higher hydraulic load translates to increased hydraulic shear stress, enabling easier detachment and removal of particles, eventually accelerating suffusion progression.

4. Results and discussion of the shearing tests

Seepage can trigger suffusion within the soil, leading to structural changes. These changes affect the arrangement of the voids and particle contacts, which in turn influence the soil's stress–strain behavior and other mechanical properties. To assess the impact of seepage on the mechanical responses, each specimen is subjected to an undrained triaxial compression shear test immediately following the seepage test. All tests are conducted with an initial mean effective stress of 50 kPa.

4.1. Effect of initial density on stress–strain behavior

First of all, an examination is made of how the initial density and C_u impact the undrained mechanical responses of non-eroded specimens. This is followed by a comparison with companion eroded specimens. To systematically quantify the undrained mechanical responses of the soils studied here, four distinct states are defined (Murthy et al., 2007): instability state (IS), phase transformation state (PT), quasi-steady state (QS), and critical state (CS). All states, but the quasi-steady state (QS), can be seen in Fig. 9. IS is the point at which shear stress reaches an initial maximum. PT is the point of transition from contractive to dilative behavior. QS is the point where shear stress reaches a local minimum. CS is the critical state at which the soil deforms at a constant void ratio and effective stress (i.e., zero change in deviator stress, $q = [\sigma'_a - \sigma'_r]/2$, and mean effective stress, $p' = [\sigma'_a + 2\sigma'_r]/3$, where σ'_a is the effective axial stress and σ'_r is the effective radial stress). In this study, the final state of the shearing tests is assumed to represent the critical state (Been et al., 1991; Murthy et al., 2007).

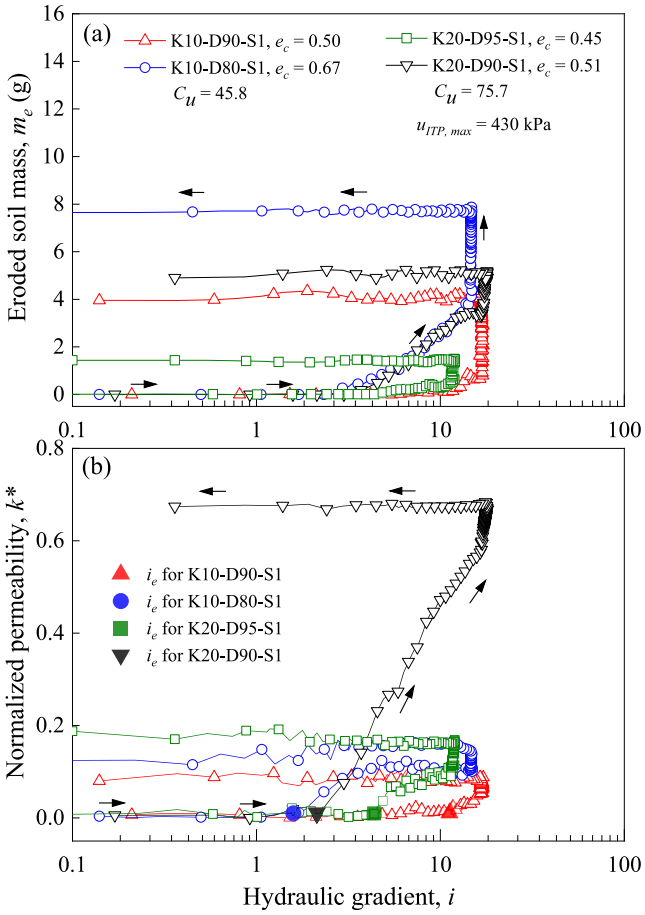

Fig. 6. Effect of initial density on the changes in eroded mass and permeability.

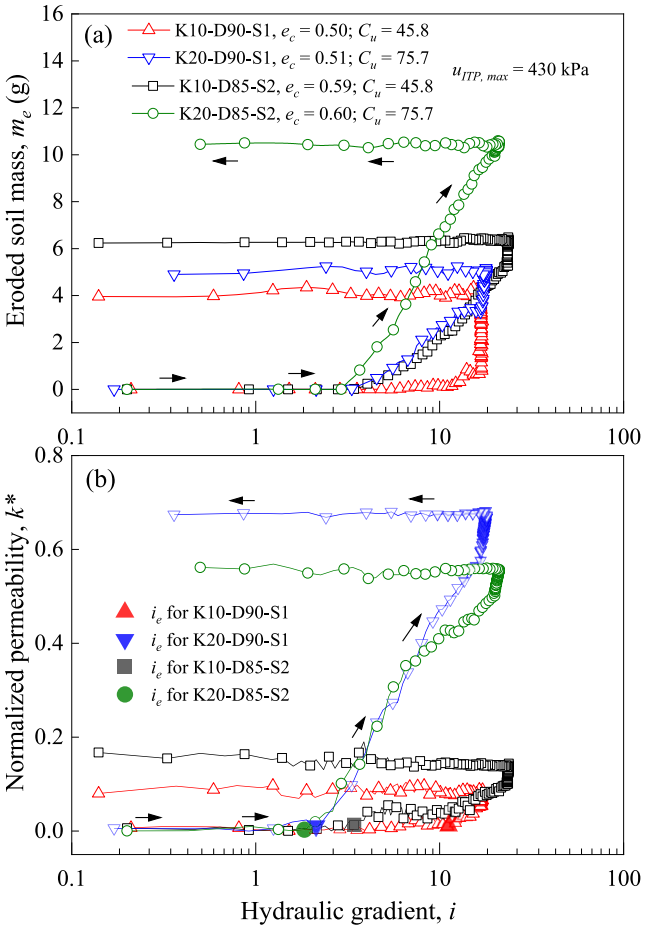

Fig. 7. Effect of uniformity coefficient on the changes in eroded mass and permeability.

Fig. 9 illustrates the stress–strain relations (deviator stress q versus axial strain ε_a) and pore-water pressure (u) responses, as well as the effective stress paths (deviator stress q versus mean effective stress p') of the non-eroded specimens. The void ratio after consolidation and the states of the undrained mechanical responses are also illustrated in this figure. The undrained triaxial compression test results are summarized in Table 5. It is noted that QS is assumed to have the same q value as PT since it is not distinguishable in the figure.

Fig. 9(a) and (b) show the distinct mechanical responses of the K10 specimens with varying densities. The densest specimen (K10-D90) exhibits strain-softening behavior with the largest strength and a dilative response. Conversely, the loosest specimen (K10-D80) also exhibits strain-softening behavior, but with the smallest strength and a contractive response. The moderately dense specimen (K10-D85) displays a unique contractive-dilative behavior, with initially decreasing and then increasing pore-water pressure. Fig. 9(a) and (c) reveal a decrease in q at IS, PT, and CS with increasing e_c. Overlaid in Fig. 9(c) are instability lines (ILs) or flow liquefaction lines, connecting the origin and the instability state in the $q - p'$ space. Notably, the ILs are not clearly distinguishable from the e_c curves, and their slope decreases with increasing e_c. This further confirms reduced liquefaction resistance with decreasing density.

Fig. 9(d) and (f) illustrate the undrained mechanical responses of the K20 specimens with varying e_c. The densest specimen (K20-D95) initially exhibits positive pore-water pressure up to a strain of 1.46 %. However, after reaching PT, the undrained stress path reverses, transitioning from contractive to dilative behavior, as shown in Fig. 9(e). Subsequently, the stress–strain response exhibits strain hardening without a distinct peak, finally reaching the CS at a large strain. This trend is consistent across all K20 specimens. Furthermore, Fig. 9(a) and (c) demonstrate that q at PT and CS increases with decreasing e_c. Conversely, Fig. 9(b) indicates that the pore-water pressures at PT and CS decrease as e_c decreases.

Fig. 9 also demonstrates the repeatability of the undrained triaxial compression test by comparing the stress–strain curves, pore-water pressure, and stress paths of specimens K20-D85 and K20-D85-R. As is evident, both specimens display virtually identical mechanical behaviors, providing strong evidence for the test's consistency and reliability.

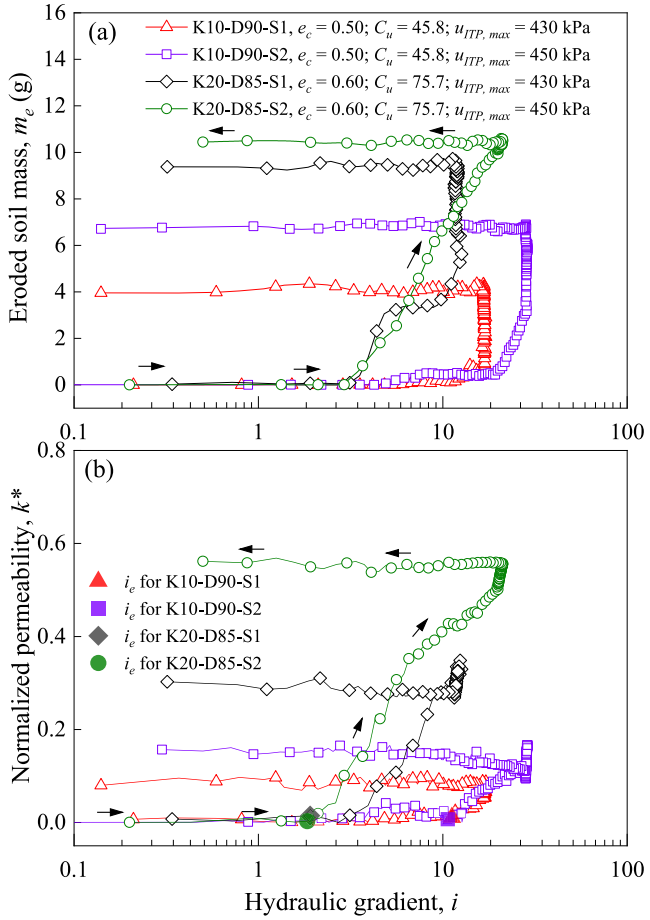

Fig. 8. Effect of hydraulic loading on the changes in eroded mass and permeability.

4.2. Effect of uniformity coefficient on stress–strain behavior

Compressive tests on the K20 soils display a unique mechanical response compared to the K10 tests. Unlike the K10 specimens, the K20 specimens exhibit strain-hardening, dilative behavior with no distinct peak strength. q at IS is not evident, but q at PT and CS decreases with e_c. Since the peak shear stress is not apparent, Ils are not indicated for the K20 tests. This highlights the significant influence of C_u on the stress–strain behavior.

To investigate the effect of C_u on the stress–strain behavior, a comparison is made between specimens K10-D85 and K20-D85. These specimens have comparable e_c and C_c, but differ significantly in their C_u. As seen in Fig. 9, the specimen with smaller C_u (K10-D85) exhibits a distinct peak shear strength and dilative response. In contrast, the specimen with larger C_u (K20-D85) lacks a clear peak strength, but still displays a dilative tendency. This is evident by the generation of negative pore-water pressure and an increase in deviatoric stress at a large axial strain.

Fig. 4 reveals insightful microscopic differences in the internal structures (fabrics) of K10-D90-S2 and K20-D90-S1. These fabric differences could be used to explain the contrasting peak strengths observed in K10-D85 and K20-D85 since they have the same gradation. The smaller C_u of K10-D85 would allow finer particles to pack around coarser ones, as shown in the images. This close interaction between particle sizes most likely contributes to the observed peak strength in its stress–strain response.

In contrast, the larger C_u of K20-D85 lacks a clear peak strength. Here, the finer particles might act as lubricants between the coarser grains during shearing, increasing compressibility rather than contributing to strength. This underscores how variations in C_u, even at the same initial density, can significantly impact stress–strain behavior.

4.3. Effect of suffusion and self-filtration on stress–strain behavior

Figs. 10 and 11 present comparisons of the results of undrained compression tests on eroded specimens to those of companion non-eroded specimens. Notably, Table 3 reveals that all key parameters, such as the B-value, initial mean effective stress (p'_i), and e_c, are nearly identical for specimens with the same C_u, except for the void ratio due to suffusion (e_e). This controlled setup allows us to isolate the impact of suffusion and self-filtration on their stress–strain curves and other mechanical responses.

The impact of suffusion and self-filtration on the K10-D80 and K10-D85 series is evident in the stress–strain curves of Fig. 10(a), while Fig. 10(d) indicates this impact on the K10-D90 series. The eroded specimens show a decrease in peak shear strength compared to their non-eroded companions. Furthermore, the eroded specimens exhibit a larger pore-water pressure generation, reaching a larger peak at medium strains and remaining constant during the PT state. This contractive behavior, shown in Fig. 10(b) for K10-D80 and K10-D85 series and Fig. 10(e) for K10-D90 series, indicates greater compressibility under undrained conditions due to enlarged voids which are likely to have been caused by particle loss and relocation. Interestingly, the K10-D90 series display the most dramatic changes in the stress–strain curves and pore-water pressure generation. The eroded specimens show a significant decrease in peak shear strength and a shift from dilative to contractive behavior compared to the non-eroded specimens. Quantitatively, the eroded specimens demonstrate smaller q at the IS, PT, and CS states compared to the non-eroded specimens. Additionally, the eroded specimens are associated with a smaller minimum mean effective stress (p'_{min}) and decreased IL slope. This decrease in the IL slope reflects a reduction in liquefaction resistance due to suffusion and self-filtration.

Unlike the K10 specimens, a distinct peak deviator stress is generally absent from the stress–strain curves for the non-eroded K20 specimens, as shown in Fig. 11. The eroded specimens have a greater peak deviator stress at medium strain and the deviator stress progressively decreases after crossing the PT state, indicating a more contractive response compared to the benchmark speci-

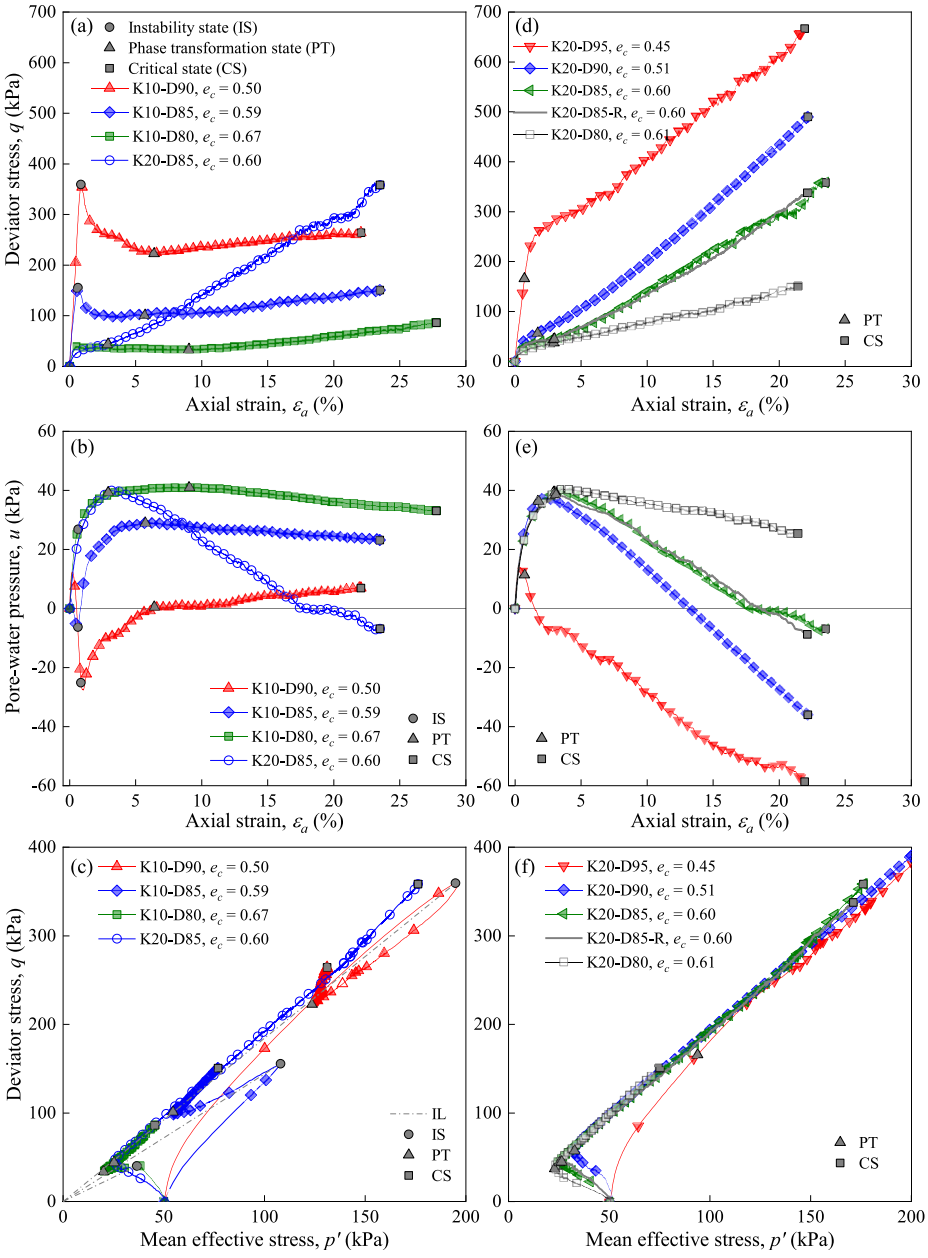

Fig. 9. Effect of initial density and uniformity coefficient on the undrained compression test results for all non-eroded specimens.

mens. q at the PT and CS states is smaller in the eroded specimens than in the non-eroded specimens. This suggests a more contractive response compared to the non-eroded specimens, potentially due to the formation of larger voids caused by suffusion and self-filtration.

Fig. 12 plots the deviator stress and pore-water pressure against axial strain at the small strain of $\varepsilon_a = 0$ %–1.2 % for the selected non-eroded (K10-D90) and eroded (K10-D90-S1 and K10-D90-S2) specimens. The eroded specimens exhibit a sudden drop in deviator stress and a sharp increase in pore-water pressure around the peak, while the non-eroded specimen does not. Suffusion can lead to unstable or collapsible soil structures within the specimen, which may collapse under axial loading. This is evidenced by the sudden reduction in stress and a sharp increase in pore-water pressure under undrained conditions, as described by Wang and Li (2015).

4.4. Effect of suffusion and self-filtration on stiffness

Fig. 13 illustrates the impact of initial density on the undrained secant stiffness (E_s). The undrained secant stiffness is the slope of a line drawn from the origin of the stress–strain curve and intersecting the curve at each stress–strain point. E_s increases as e_c decreases, indicating the influence of the packing conditions on soil stiffness. The stiffness increases with density (i.e., decreasing void ratio) and is consistent with numerous previous studies

Table 5
Summary of the undrained triaxial compression test results.

Test code	Pre-shearing conditions				Instability state (IS) or peak				Phase transformation state (PT)				Critical state (CS)			
	B-value	p'_i (kPa)	e_c	e_e	$\varepsilon_{a,p}$ (%)	q_p (kPa)	p'_p (kPa)	u_p (kPa)	$\varepsilon_{a,pt}$ (%)	q_{pt} (kPa)	p'_{pt} (kPa)	u_{pt} (kPa)	$\varepsilon_{a,cs}$ (%)	q_{cs} (kPa)	p'_{cs} (kPa)	u_{cs} (kPa)
K10-D80	0.98	50	0.67	–	0.6	40	37	27	9.0	34	20	41	27.8	86	46	33
K10-D85	0.97	50	0.59	–	0.6	155	108	−6	5.7	101	55	29	23.5	150	77	23
K10-D90	0.97	50	0.50	–	0.9	359	195	−25	6.4	223	124	0	22.1	264	131	7
K10-D80-S1	0.99	50	0.67	0.68	1.0	31	29	31	6.7	26	14	44	23.2	52	29	38
K10-D85-S2	0.97	50	0.59	0.60	0.5	106	77	8	7.1	82	46	31	22.3	116	61	28
K10-D90-S1	1.00	50	0.50	0.51	0.4	135	85	10	2.8	6	2	50	23.0	44	22	43
K10-D90-S2	1.00	50	0.50	0.51	0.5	107	70	16	3.9	17	6	50	26.0	62	27	44
K20-D80	0.99	50	0.61	–	–	–	–	–	2.9	37	23	39	21.4	151	75	25
K20-D85	1.00	50	0.60	–	–	–	–	–	2.9	44	25	39	23.5	358	176	−7
K20-D85-R	0.99	50	0.60	–	–	–	–	–	3.0	45	27	38	22.1	338	171	−9
K20-D90	1.00	50	0.51	–	–	–	–	–	1.7	57	33	36	22.2	490	249	−36
K20-D95	0.98	50	0.45	–	–	–	–	–	0.7	166	94	11	21.9	667	331	−59
K20-D85-S1	1.00	50	0.60	0.62	1.2	26	25	34	3.7	24	19	40	22.0	77	42	34
K20-D85-S2	1.00	50	0.60	0.61	1.0	23	26	32	4.3	22	17	40	22.4	91	46	34
K20-D90-S1	1.00	50	0.51	0.52	1.1	36	31	31	5.4	28	18	41	22.7	75	39	36
K20-D95-S1	0.99	50	0.45	0.46	–	–	–	–	1.1	172	92	15	26.8	471	240	–33

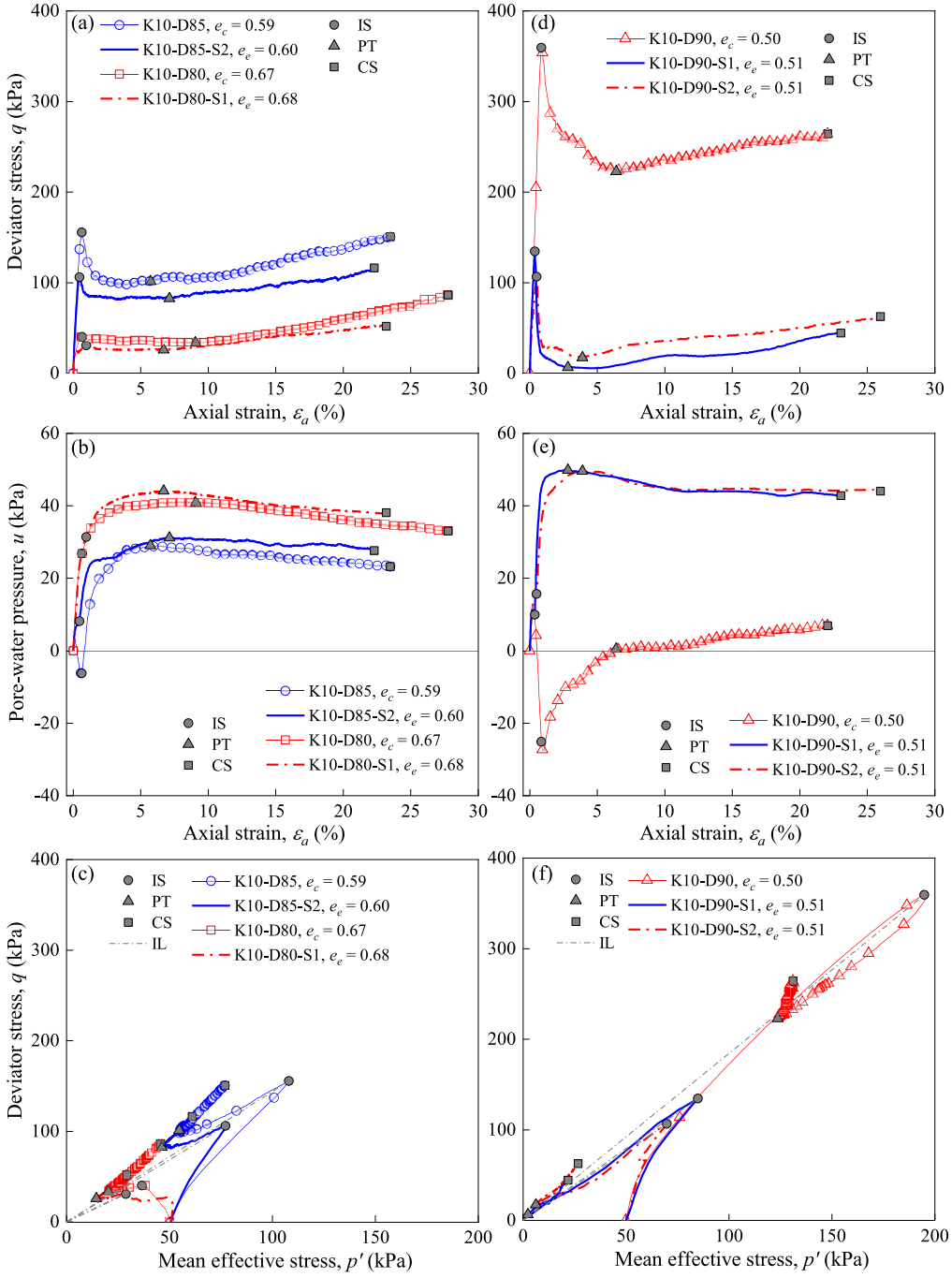

Fig. 10. Effect of suffusion and self-filtration on the undrained compression tests for the K10 test series.

(e.g., Kramer and Seed, 1988; Konrad, 1990; Yoshimine and Ishihara, 1998; Chu and Leong, 2004).

In Fig. 13, E_s is also compared between the eroded and non-eroded specimens. Generally speaking, the eroded specimens exhibit smaller stiffness compared to their companions. However, K20-D95-S1, characterized by a high initial density, experiences insignificant particle erosion, resulting in a slight decrease in stiffness. The general trend of lower stiffness in eroded soils can be attributed to the detachment and relocation of finer particles, which contribute significantly to soil stiffness.

4.5. Effect of suffusion and self-filtration on particle-size distribution and shear deformation

After the undrained compression tests, the specimens are split into three equal sections and the PSDs of each section are determined. For instance, Fig. 14 illustrates the selected PSDs of the K10-D85-S2 and K20-D85-S2 specimens before and after the tests, along with the eroded soil. The total eroded masses collected in the collector are 5.8 g and 10.1 g for K10-D85-S2 and K20-D85-S2, respectively. The percentage of particles finer than 0.15 mm and

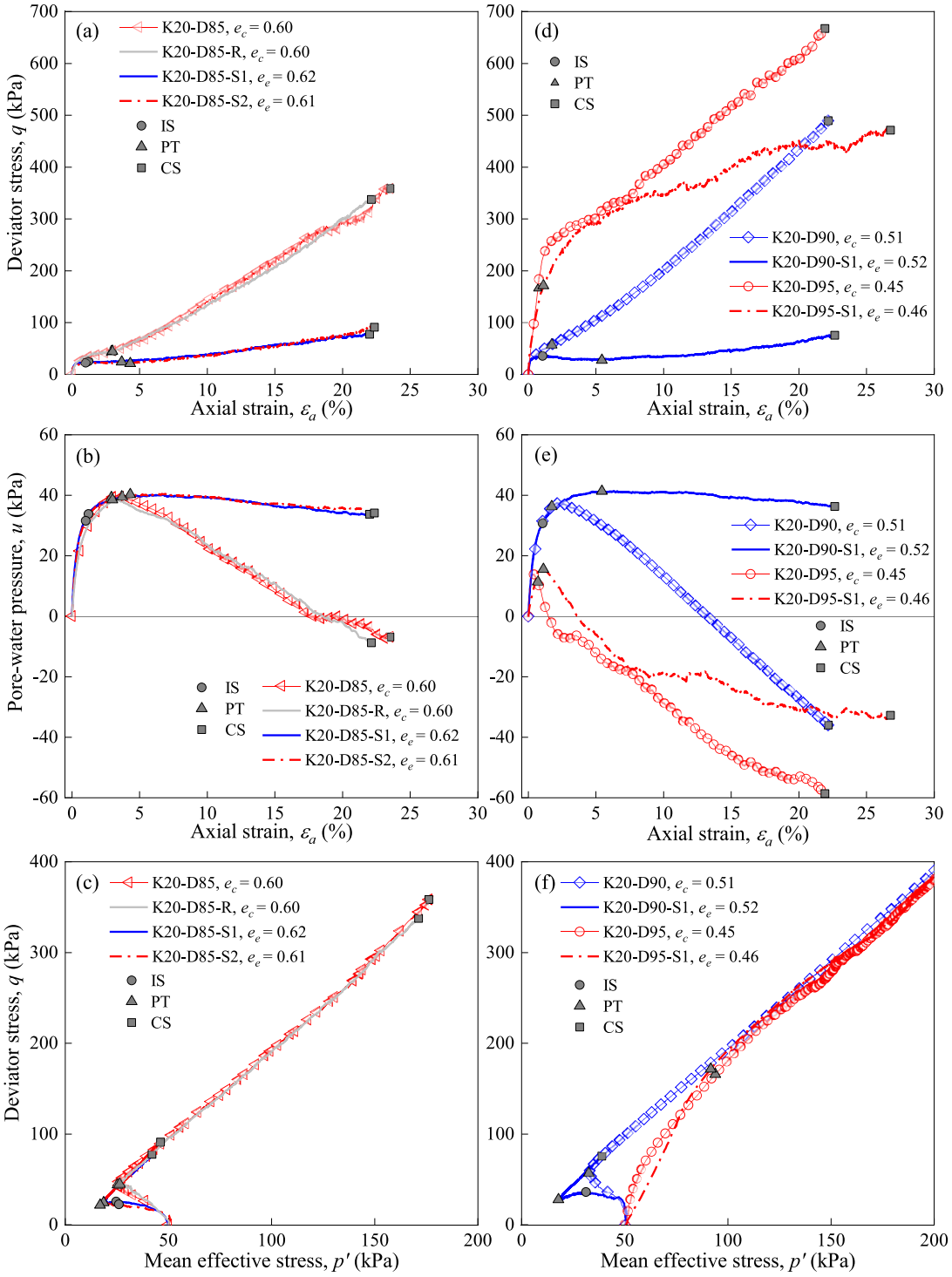

Fig. 11. Effect of suffusion and self-filtration on the undrained compression tests for the K20 test series.

0.25 mm (the largest fine particles) are 87.3 % and 86.4 % for K10-D85-S2 and K20-D85-S2, respectively. At the top of both specimens, there is a significant decrease (about 6.5 % – 20.3 %) in the mass percentage of particles with diameters between 0.063 mm and 0.425 mm. Conversely, the middle sections show an increase (about 4.7 % – 9.6 %) in this size range. The minimal change is observed in the bottom section. This suggests that particles eroded from the top migrate and become lodged in the middle zone. This migration leads to a non-uniform PSD throughout the specimen, potentially resulting in a larger void ratio in the top portion.

Fig. 15 shows the initial specimen diameter profile and the profile at the end of shearing for the non-eroded (K10-D85 and K20-D85-R) and eroded (K10-D85-S2 and K20-D85-S2) specimens. The initial and end-of-

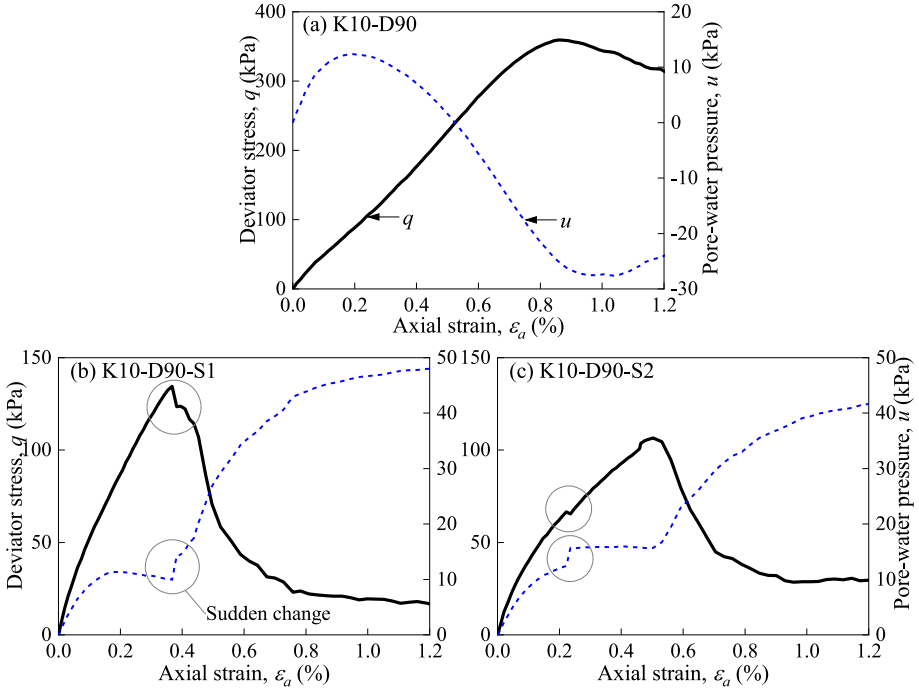

Fig. 12. Changes in deviator stress and pore-water pressure against axial strain at small axial strain: (a) K10-D90, (b) K10-D90-S1, and (c) K10-D90-S2.

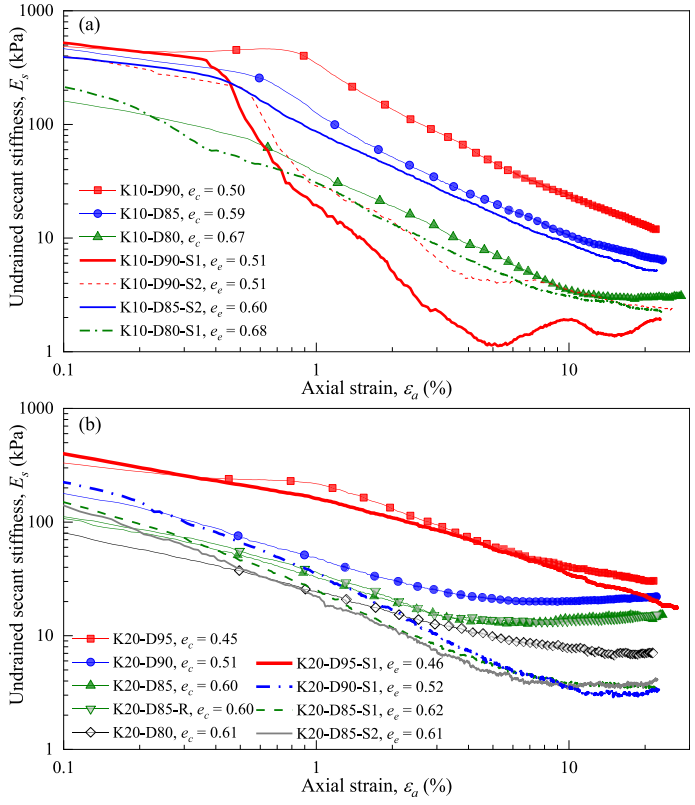

Fig. 13. Effect of suffusion and self-filtration on undrained secant stiffness for (a) K10 test series and (b) K20 test series.

shearing profiles are determined by the specimen diameters measured at the clip gauge locations, recorded after specimen preparation and shearing, respectively. The top and base specimen diameters correspond to the diameters of the top cap and base pedestal, respectively. It is seen that the non-eroded specimens bulge outwards with the largest

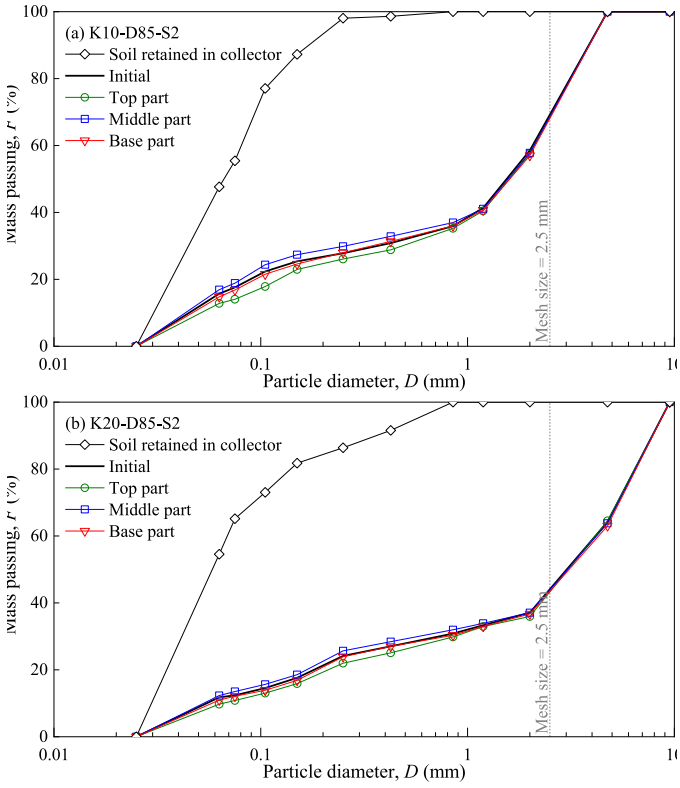

Fig. 14. Post-test particle-size distribution curves for (a) K10-D85-S2 and (b) K20-D85-S2.

deformation occurring in the middle part of the specimens. This is expected for a specimen with a uniform PSD and void ratio before the compression test. However, the eroded specimens have larger deformation in the top part, probably due to local clogging, resulting in the non-uniform distribution of particles and a possible larger void ratio in the top part. Consequently, this makes the top part weaker and more prone to deformation. Further investigation is required to understand this aspect in greater detail.

4.6. Effect of suffusion and self-filtration on critical state

Upon experiencing suffusion, a specimen undergoes particle rearrangement, resulting in modifications to its PSD and e throughout the specimen length (Nguyen et al., 2019). Consequently, the critical state lines (CSLs) in the compression plane (v – log p') are significantly altered (Muir Wood et al., 2010; Li et al., 2024). The CSL in the v – log p' space can be expressed as follows:

$$v = \Gamma - \lambda \ln p' \tag{5}$$

where v is the specific volume ($v = 1 + e_c$), and Γ and λ are the intercept with 1 kPa and slope of CSL, respectively. The CSL is defined using critical state (CS) data points obtained at the end of the shearing tests on each specimen (Been et al., 1991; Murthy et al., 2007).

Under undrained conditions, the void ratio remains constant, meaning that the effective stress decreases and eventually reaches the critical state. Fig. 16 shows the critical state points for all the cases on the v-log p' plane. As shown in this figure, all the tests on the non-eroded K10 specimens with different v fall on the same critical state line. The same goes for the non-eroded K20 specimens. The CSL for each soil type has different Γ and λ values. This means that the location of the CSL depends on the soil's PSD. The values for λ are 0.162 and 0.165, and those for Γ are 2.293 and 2.429, for the K10 and K20 specimens, respectively. The fitted CSLs exhibit high coefficients of determination (R^2) with values of 0.999 and 0.947, respectively. The difference in λ seems to be negligible and only the difference in Γ is seen (Been and Jefferies, 1985; Ciantia et al., 2019).

Fig. 16 also shows the changes in the critical state due to suffusion and self-filtration. The filled symbols indicate the

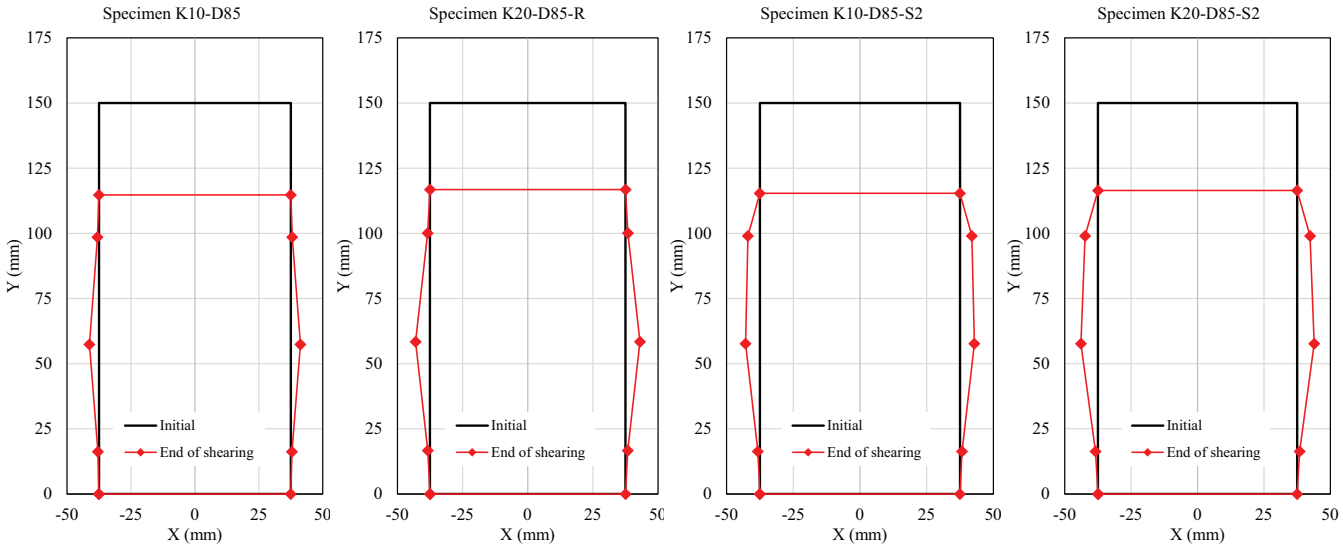

Fig. 15. Specimen profiles after preparation and at the end of shearing.

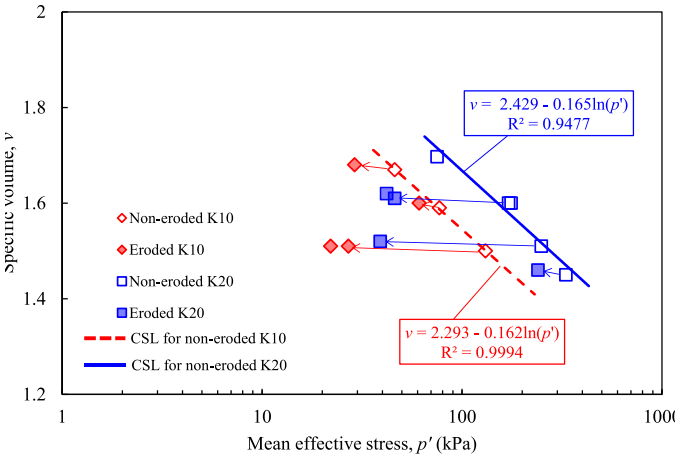

Fig. 16. Critical state of the tests on the specific volume – mean effective stress plane.

critical state points of the eroded specimens, and their mean effective stress at the critical state is smaller than that for the non-eroded specimens. This smaller mean effective stress at the critical state indicates that the soil state changes to the looser state. This disparity highlights the weakening effect of suffusion and self-filtration on the soil at its critical state.

In this study, the changes in mean effective stress ($\Delta p'_{cs,e}$) and specific volume (Δv_e) at the critical state, due to suffusion and self-filtration, are introduced to describe the effects of suffusion and self-filtration on the critical state of the soil. $\Delta p'_{cs,e}$ is defined as the difference in mean effective stress at the critical state of non-eroded soil ($p'_{cs,n}$) and the mean effective stress at the critical state of eroded soil ($p'_{cs,e}$), calculated from the equations shown in Fig. 16. Δv_e is defined as the difference in specific volume after consolidation (v_c) and specific volume after suffusion and self-filtration (v_e). The values for $\Delta p'_{cs,e}$, $p'_{cs,n}$, $p'_{cs,e}$, $\Delta \boldsymbol{v_e}$, v_c, and v_e are listed in Table 6. Although the variation in Δv_e is minimal, $\Delta p'_{cs,e}$ exhibits inconsistency, indicating a significant change in mean effective stress at the critical state. The stress–strain behavior of sands at the critical state is primarily controlled by the global void ratio or density (Been et al., 1991). However, the relatively small change in specific volume (or void ratio), caused by the suffusion and self-filtration in these well-graded soils, leads to a marked change in mean effective stress at the critical state. This suggests that the global void ratio is not a reliable predictor of critical state stress–strain behavior in well-graded sands affected by suffusion and self-filtration. The significant change in mean effective stress at the critical state is tentatively linked to the development of heterogeneous voids and particle-size distributions along the specimen due to suffusion and self-filtration. This heterogeneity most likely causes well-graded soils to become looser, thus exhibiting more contractive behavior at large shear strains, consistent with the findings of Prasomsri and Takahashi (2020, 2021). Further investigation into the stress–strain behavior of soils experiencing suffusion and self-filtration, potentially using techniques such as discrete element modeling, is crucial for understanding the undrained mechanical behavior of well-graded soils undergoing these processes.

5. Conclusions

Series of seepage tests were carried out on two well-graded soils to investigate the effects of the initial density, uniformity coefficient, and hydraulic loading amplitude on suffusion. Subsequent undrained triaxial compression tests were performed to investigate the impact of suffusion on the stress–strain behavior. The major findings obtained in this study are as follows:

- Well-graded soils, despite being identified as internally unstable to suffusion based on gradation shape criteria, can still resist erosion due to self-filtration, especially when the uniformity coefficient is low and the initial density is high. This highlights the limitations of these criteria and underscores the need for the experimental characterization of soil erodibility.
- Suffusion and self-filtration characteristics, particularly the hydraulic gradient initiating erosion and changes in permeability, are influenced by the initial density, uniformity coefficient, and hydraulic loading. A higher initial density and smaller uniformity coefficient lead to a

Table 6
Changes in the specific volume and mean effective stress at te critical state due to suffusion and self-filtration.

Test code	v_c	v_e	$\Delta v_e = v_e - v_c$	$p'_{cs,n}$ (kPa)	$p'_{cs,e}$ (kPa)	$\Delta p'_{cs,e} = p'_{cs,e} - p'_{cs,n}$ (kPa)
K10-D80-S1	1.67	1.68	0.01	47	29	18
K10-D85-S2	1.59	1.60	0.01	77	61	16
K10-D90-S1	1.50	1.51	0.01	134	22	112
K10-D90-S2	1.50	1.51	0.01	134	27	107
K20-D85-S1	1.60	1.62	0.02	152	42	110
K20-D85-S2	1.60	1.61	0.01	152	46	106
K20-D90-S1	1.51	1.52	0.01	262	39	223
K20-D95-S1	1.45	1.46	0.01	377	240	137

Note: v_c = specific volume after consolidation; v_e = specific volume after suffusion and self-filtration; Δv_e = change in specific volume due to suffusion; $p'_{cs,n}$ = mean effective stress at critical state of non-eroded soil (calculated from equations shown in Fig. 16); $p'_{cs,e}$ = mean effective stress at critical state of eroded soil; $\Delta p'_{cs,e}$ = change in $p'_{cs,e}$ from critical state of non-eroded soil.

higher hydraulic gradient initiating erosion. Additionally, changes in permeability increase significantly with increasing hydraulic loading amplitude.
- Suffusion and self-filtration significantly alter the stress–strain behavior and key mechanical properties of the soils. These processes result in a decrease in peak strength, stiffness, and a more contractive behavior due to relocation and clogging. Additionally, they also lead to a smaller mean effective stress at the critical state in the relationship between specific volume and mean effective stress.

Suffusion and self-filtration can cause severe problems in the internal stability state of soils, based on the observed reduction in strength and stiffness. The authors have highlighted the importance of conducting laboratory testing to determine the impact of suffusion on shear strength to assess the internal stability of earth structures.

CRediT authorship contribution statement

Jitrakon Prasomsri: Writing – original draft, Visualization, Methodology, Investigation, Conceptualization. **Ratamanee Nuntasarn:** Writing – review & editing. **Suched Likitlersuang:** Writing – review & editing. **Akihiro Takahashi:** Writing – review & editing, Supervision, Methodology, Funding acquisition, Conceptualization.

Acknowledgments

The first author gratefully acknowledges the scholarship support of the Japanese Government (Monbukagakusho: MEXT). This work was partially supported by JSPS KAKENHI Grant Nos. 19H02232 and 23K26193.

References

ASTM D2434-19, 2019. Standard test method for permeability of granular soils (constant head), Annual Book of ASTM Standards, Vol. 04.08, ASTM International, West Conshohocken.
ASTM D2487-11, 2012. Standard practice for classification of soils for engineering purposes (Unified Soil Classification System). Annual Book of ASTM Standards. ASTM International, West Conshohocken, PA.
ASTM D4767-11, 2012. Standard test method for consolidated undrained triaxial compression test for cohesive soils, Annual Book of ASTM Standards, Vol. 04.08, ASTM International, West Conshohocken.
ASTM D5084-10, 2010. Standard test methods for measurement of hydraulic conductivity of saturated porous materials using a flexible wall permeameter. Annual Book of ASTM Standards. ASTM International, West Conshohocken, PA.
ASTM D7181-20, 2020. Test method for consolidated drained triaxial compression test for soils, Annual Book of ASTM Standards, Vol. 04.08, ASTM International, West Conshohocken.
ASTM E2655-08, 2008. Standard guide for reporting uncertainty of test results and use of the term measurement uncertainty in ASTM test methods. Annual Book of ASTM Standards. ASTM International, West Conshohocken, PA.
Bandini, P., Sathiskumar, S., 2009. Effects of silt content and void ratio on the saturated hydraulic conductivity and compressibility of sand-silt mixtures. J. Geotech. Geoenviron. Eng. 135 (12), 1976–1980.
Been, K., Jefferies, M.G., Hachey, J., 1991. The critical state of sands. Geotechnique 41 (3), 365–381.
Been, K., Jefferies, M.G., 1985. A state parameter for sands. Géotechnique 35 (2), 99–112.
Belkhatir, M., Schanz, T., Arab, A., 2013. Effect of fines content and void ratio on the saturated hydraulic conductivity and undrained shear strength of sand–silt mixtures. *Environ. Earth Sci.* 70 (6), 2469–2479.
Chang, D.S., Zhang, L.M., 2011. A stress-controlled erosion apparatus for studying internal erosion in soils. *Geotech. Test. J.* 34 (6), 579–589.
Chen, C., Zhang, L., 2023. Hydro-mechanical behaviour of soil experiencing seepage erosion under cyclic hydraulic gradient. *Géotechnique* 73 (2), 115–127.
Chitravel, S., Otsubo, M., Kuwano, R., 2021. Experimental study on stiffness degradation and monotonic response of reconstituted volcanic ash induced by internal erosion. *Soils Found.* 61 (5), 1431–1452.
Chu, J., Leong, W.K., 2004. Effect of fines on instability behaviour of loose sand. *Géotechnique* 52 (10), 751–755.
Ciantia, M.O., Arroyo, M., O'Sullivan, C., Gens, A., Liu, T., 2019. Grading evolution and critical state in a discrete numerical model of Fontainebleau sand. *Géotechnique* 69 (1), 1–15.
Douglas, K.J., Fell, R., Peirson, W.L., Studholme, H., 2019. Experimental investigation of global backward erosion and suffusion of soils in embankment dams. *Can. Geotech. J.* 56 (6), 789–807.
Fannin, R.J., Slangen, P., 2014. On the distinct phenomena of suffusion and suffosion. Géotechnique Lett. 4 (4), 289–294.
Fell, R., Wan, C.F., Cyganiewicz, J., Foster, M., 2003. Time for development of internal erosion and piping in embankment dams. *J. Geotech. Geoenviron. Eng.* 129 (4), 307–314.
Foster, M., Fell, R., 2001. Assessing embankment dam filters that do not satisfy design criteria. J. Geotech. Geoenviron. Eng. 127 (5), 398–407.
Johnston, I., Murphy, W., Holden, J., 2024. The effects of internal erosion on granular soils used in transport embankments. *Soils Found.* 64 (1) 101424.
Jiang, M.J., Konrad, J.M., Leroueil, S., 2003. An efficient technique for generating homogeneous specimens for DEM studies. *Comput. Geotech.* 30 (7), 579–597.
Kafui, K.D., Thornton, C., Adams, M.J., 2002. Discrete particle-continuum fluid modelling of gas–solid fluidised beds. *Chem. Eng. Sci.* 57 (13), 2395–2410.
Ke, L., Takahashi, A., 2014. Triaxial erosion test for evaluation of mechanical consequences of internal erosion. Geotech. Testing J 37 (2) 20130049.
Ke, L., Takahashi, A., 2015. Drained monotonic responses of suffusional cohesionless soils. *J. Geotech. Geoenviron. Eng.* 141 (8) 04015033.
Kenney, T.C., Lau, D., 1985. Internal stability of granular filters. *Can. Geotech. J.* 22 (2), 215–225.
Kenney, T.C., Lau, D., 1986. Internal stability of granular filters: Reply. *Can. Geotech. J.* 23 (3), 420–423.
Konrad, J.M., 1990. Minimum undrained strength of two sands. *J. Geotech. Eng.* 116 (6), 932–947.
Kramer, S.L., Seed, H.B., 1988. Initiation of soil liquefaction under static loading conditions. *J. Geotech. Eng.* 114 (4), 412–430.
Krumbein, W.C., Monk, G.D., 1943. Permeability as a function of the size parameters of unconsolidated sand. *Trans. AIME* 151 (01), 153–163.
Ladd, R., 1978. Preparing test specimens using undercompaction. Geotech. Test. J., ASTM Int., West Conshohocken, PA 1 (1), 16–23.
Lafleur, J., Nguyen, P.H., 2007. Internal stability of particles in dam cores made of cohesionless broadly graded moraines, Internal Erosion of Dams and their Foundations. Taylor and Francis, London, pp. 151–158.
Le, V.T., Marot, D., Rochim, A., Bendahmane, F., Nguyen, H.H., 2018. Suffusion susceptibility investigation by energy-based method and statistical analysis. *Can. Geotech. J.* 55 (1), 57–68.
Li, S., Russell, A.R., Muir Wood, D., 2024. Internal erosion of a gap-graded soil and influences on the critical state. *Acta Geotech.*, 1–19.
Li, S., Russell, A.R., Muir Wood, D., 2020. Influence of particle-size distribution homogeneity on shearing of soils subjected to internal erosion. *Can. Geotech. J.* 57 (11), 1684–1694.
Mehdizadeh, A., Disfani, M.M., Evans, R., Arulrajah, A., Ong, D.E.L., 2017. Mechanical consequences of suffusion on undrained behaviour

of a gap-graded cohesionless soil-an experimental approach. *Geotech. Test. J.* 40 (6), 1026–1042.
Muir Wood, D.M., Maeda, K., Nukudani, E., 2010. Modelling mechanical consequences of erosion. *Géotechnique* 60 (6), 447–457.
Murthy, T.G., Loukidis, D., Carraro, J.A.H., Prezzi, M., Salgado, R., 2007. Undrained monotonic response of clean and silty sands. Géotechnique 57 (3), 273–288.
Nguyen, C.D., Benahmed, N., Andò, E., Sibille, L., Philippe, P., 2019. Experimental investigation of microstructural changes in soils eroded by suffusion using X-ray tomography. Acta Geotech. 14 (3), 749–765.
Nguyen, T.T., Indraratna, B., 2020. A coupled CFD–DEM approach to examine the hydraulic critical state of soil under increasing hydraulic gradient. *Int. J. Geomech.* 20 (9) 04020138.
Ouyang, M., Takahashi, A., 2015. Influence of initial fines content on fabric of soils subjected to internal erosion. *Can. Geotech. J.* 53 (2), 299–313.
Peng, M., Zhang, L.M., 2012. Breaching parameters of landslide dams. *Landslides* 9 (1), 13–31.
Prasomsri, J., Takahashi, A., 2020. The role of fines on internal instability and its impact on undrained mechanical response of gap-graded soils. *Soils Found.* 60 (6), 1468–1488.
Prasomsri, J., Takahashi, A., 2021. Experimental study on suffusion under multiple seepages and its impact on undrained mechanical responses of gap-graded soil. *Soils Found.* 61 (6), 1660–1680.
Prasomsri, J., Shire, T., Takahashi, A., 2021. Effect of fines content on onset of internal instability and suffusion of sand mixtures. *Géotechnique Lett.* 11 (3), 209–214.
Razavi, S.K., Hajialilue Bonab, M., Dabaghian, A., 2020. Investigation into the internal erosion and local settlement of Esfarayen Earth-Fill dam. *J. Geotech. Geoenviron. Eng.* 146 (4) 04020006.
Rochim, A., Marot, D., Sibille, L., Thao Le, V., 2017. Effects of hydraulic loading history on suffusion susceptibility of cohesionless soils. *J. Geotech. Geoenviron. Eng.* 143 (7) 04017025.
Sato, M., Kuwano, R., 2016. Effects of internal erosion on mechanical properties evaluated by triaxial compression tests. *Jpn. Geotech. Soc. Special Publ.* 2 (29), 1056–1059.
Shire, T., O'Sullivan, C., Hanley, K.J., Fannin, R.J., 2014. Fabric and effective stress distribution in internally unstable soils. J. Geotech. Geoenviron. Eng. 140 (12) 04014072.
Sibille, L., Marot, D., Sail, Y., 2015. A description of internal erosion by suffusion and induced settlements on cohesionless granular matter. *Acta Geotech.* 10 (6), 735–748.
Skempton, A.W., Brogan, J.M., 1994. Experiments on piping in sandy gravels. Geotechnique 44 (3), 449–460.
Slangen, P., Fannin, R.J., 2017. A flexible wall permeameter for investigating suffusion and suffosion. Geotech. Test. J. 40 (1), 1–14.
Stewart, R.A., Watts, B.D., 2000. The WAC Bennett dam sinkhole incident. In: Proceedings 53rd Canadian Geotechnical Conference, Montreal, Canada.
Varadarajan, A., Sharma, K.G., Venkatachalam, K., Gupta, A.K., 2003. Testing and modeling two rockfill materials. J. Geotech. Geoenviron. Eng. 129 (3), 206–218.
Wan, C.F., Fell, R., 2004. Experimental investigation of internal instability of soils in embankment dams and their foundations. University of New South Wales, School of Civil and Environmental Engineering.
Wang, X., Li, J., 2015. On the degradation of granular materials due to internal erosion. *Acta Mechanica Sinica* 31, 685–697.
Xiao, M., Shwiyhat, N., 2012. Experimental investigation of the effects of suffusion on physical and geomechanic characteristics of sandy soils. *Geotech. Test. J.* 35 (6), 890–900.
Yin, Y., Cui, Y., Tang, Y., Liu, D., Lei, M., Chan, D., 2021. Solid–fluid sequentially coupled simulation of internal erosion of soils due to seepage. *Granul. Matter* 23 (2), 20.
Yasuda, S., Shimizu, Y., Deguchi, K., 2016. Investigation of the mechanism of the 2015 failure of a dike on Kinu River. *Soils Found.*, Elsevier 56 (4), 581–592.
Yoshimine, M., Ishihara, K., 1998. Flow potential of sand during liquefaction. *Soils Found.* 38 (3), 189–198.
Zhong, C., Le, V.T., Bendahmane, F., Marot, D., Yin, Z.Y., 2018. Investigation of spatial scale effects on suffusion susceptibility. *J. Geotech. Geoenviron. Eng.* 144 (9) 04018067.